---

**Article:**
Saxton, H. orcid.org/0000-0001-7433-6154, Taylor, D.J. orcid.org/0000-0003-1068-1236, Xu, X. orcid.org/0000-0002-9721-9054 et al. (9 more authors) (2025) Derivation and sensitivity analysis of a novel one-dimensional model of coronary blood flow accounting for vessel taper & boundary slip. American Journal of Physiology-Heart and Circulatory Physiology. ajpheart.00187.2025. ISSN: 0363-6135

https://doi.org/10.1152/ajpheart.00187.2025

---

# Graphical Abstract

## Derivation and Sensitivity Analysis of a Novel One-Dimensional Model of Coronary Blood Flow Accounting for Vessel Taper & Boundary Slip

Harry Saxton, Daniel J Taylor, Xu Xu, Andrew J. Narracott, Krzysztof Czechowicz, Tom Newman, Rebecca Gosling, David R Hose, Leif Rune Hellevik, Julian P Gunn, Paul D Morris, Ian Halliday

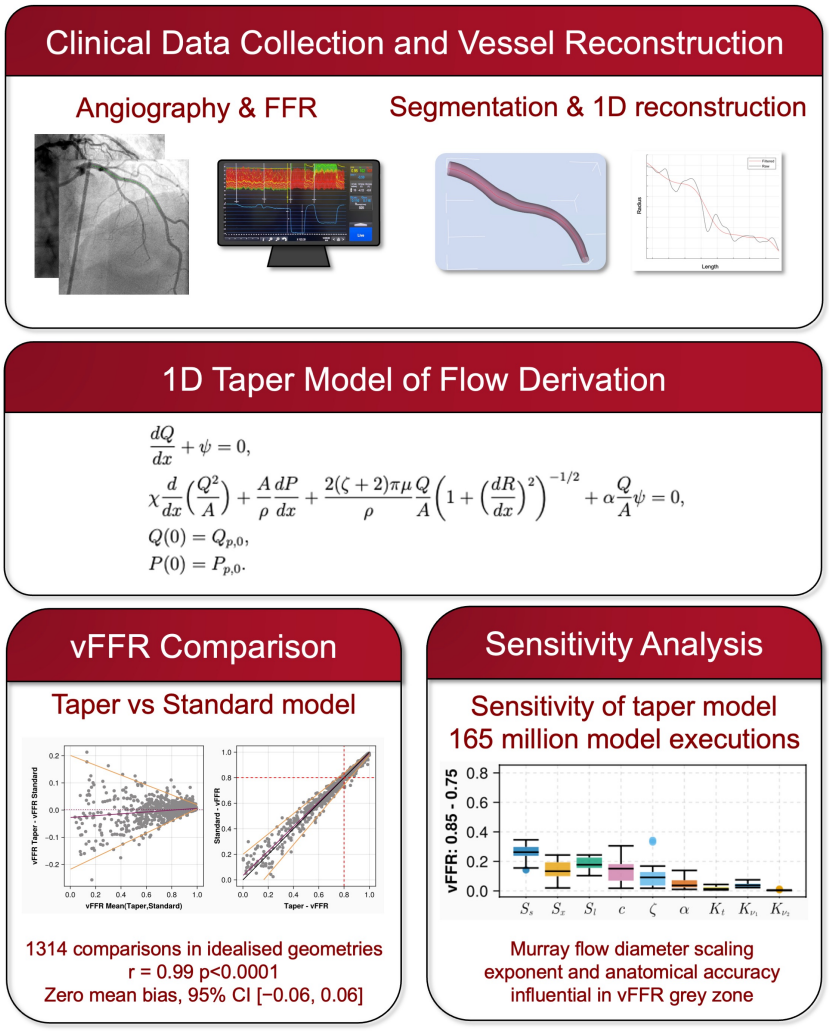

# Derivation and Sensitivity Analysis of a Novel One-Dimensional Model of Coronary Blood Flow Accounting for Vessel Taper & Boundary Slip

Harry Saxton[a,b,*], Daniel J Taylor[b,c,*], Xu Xu[a,b], Andrew J. Narracott[b,c], Krzysztof Czechowicz[b,c], Tom Newman[b,c,d,e], Rebecca Gosling[b,c,d,e], David R Hose[c], Leif Rune Hellevik[f], Julian P Gunn[b,c,d,e], Paul D Morris[b,c,d,e], Ian Halliday[b,c]

[a]*Department of Computer Science, University of Sheffield, Sheffield, United Kingdom*
[b]*Insigneo Institute for In Silico Medicine, University of Sheffield, Sheffield, United Kingdom*
[c]*Division of Clinical Medicine, School of Medicine & Population Health, University of Sheffield, Sheffield, United Kingdom*
[d]*Department of Cardiology, Sheffield Teaching Hospitals NHS Foundation Trust, Sheffield, United Kingdom*
[e]*NIHR Sheffield Biomedical Research Centre, Sheffield Teaching Hospitals NHS Foundation Trust, Sheffield, United Kingdom*
[f]*Division of Biomechanics, Department of Structural Engineering, Norwegian University of Science and Technology (NTNU), Trondheim, Norway*

## Abstract

Computational models of coronary flow allow quantification of virtual fractional flow reserve (vFFR) and absolute flow, reducing the need for invasive testing in supporting a diagnosis of ischaemic heart disease (IHD). One-dimensional (1D) models of coronary flow are an emerging tool, which provide rapid assessment of coronary physiology. However, they currently do not fully account for side branch flow, the importance of which for clinically indeterminate cases is disputed. In the current study, we derive a novel 1D model of coronary flow from the Navier-Stokes equations, which accounts for vessel taper, convective acceleration and boundary slip. Using 15 idealised coronary arterial anatomies derived from patient data, we compared

*Authors contributed equally.
**Corresponding Author daniel.taylor@sheffield.ac.uk.
Running Head: 1D Coronary Blood Flow: Taper, Slip, and Sensitivity

*Preprint submitted to American Journal of Physiology Heart and Circulatory Physiology*

vFFR results from our model with those from a pre-existing 1D model of coronary flow. The techniques showed strong correlation (r=0.99, $p < 0.001$) with close agreement. Through a novel output-constrained global sensitivity analysis (GSA), we demonstrated that anatomical parameters, particularly the magnitude of simulated side branches significantly influences vFFR in the diagnostic grey zone (0.75 - 0.85) and absolute coronary flow regardless of stenosis severity. This challenges the commonly accepted dominance of stenosis parameters. We present a more mathematically and anatomically consistent 1D system for modelling coronary flow, which demonstrated modest differences with established models. GSA highlighted the influence of the flow diameter (Murray) scaling exponent in all cases when computing flow and in intermediate epicardial stenoses when quantifying vFFR. This work highlights the importance of accurately quantifying side branch flow when computing virtual coronary physiology.

**New & Noteworthy**: A new 1D model for blood flow is derived accounting for vessel taper, side branch flow and boundary slip. This model is applied to a novel output-constrained GSA, highlighting the influence of anatomical and flow input parameters within clinically relevant regions of virtual fractional flow reserve. Notably, we reveal the significant influence of the flow diameter scaling exponent in the virtual fractional flow reserve grey zone (0.75-0.85) compared to the conventionally accepted stenosis severity.

*Keywords:* Coronary Artery Disease, Sobol Indices, vFFR, Absolute Flow, Modelling Assumptions

---

## 1. Introduction

Ischaemic heart disease frequently results from occlusive epicardial coronary artery disease (CAD). Clinically, epicardial lesion severity is often judged from angiographic appearances alone. In cases of intermediate stenoses, where images alone are inconclusive, proportional translesional flow loss may be quantified with invasive assessment of fractional flow reserve (FFR). Invasively assessed FFR is the current gold standard diagnostic technique for epicardial lesions [1] and is associated with improved patient outcomes versus angiography guided revascularisation [2]. However, FFR quantifies only proportional flow reduction and cannot assess coronary microvasculature dysfunction (CMD). Currently, microvascular assessment requires further inva-

sive assessment of coronary microvasculature resistance (CMR) [3] with either bolus thermodilution or Doppler velocity. However, agreement between techniques is poor [4], whilst increasing procedural time, cost and risk of complications.

Mathematical models of coronary physiology provide an alternative to invasive assessment. Computational fluid dynamics (CFD) workflows typically use clinical imaging to produce CFD boundary conditions representative of patient anatomy. The first CFD tools used plane [5] and CT [6] angiography to derive virtual FFR (vFFR) based on both imaging modalities (which are now commercially available [7, 8, 9]). Subsequent refinement of CFD techniques facilitate the quantification of absolute flow (mL/min), CMR [10, 11] and wall shear stress (WSS) [12]. However, such measures of coronary physiology are absolute (rather than proportional); results are therefore more sensitive, both to boundary conditions and the model of flow- including any account of side branch flow [13]. Some models include side branches in their geometrical reconstructions [11, 14, 15] and while the inclusion of a selected number of major side branches is feasible and has now translated into clinically available workflows [9], the selection of which side branches to include is subjective. Furthermore, incorporation of all major side branches in a heavily tapering vessel (most applicable to the LAD) prolongs segmentation time and increases simulation expense, which may preclude real-time use in the cardiac catheterisation laboratory. This approach also ignores smaller side branches (typically $< 1mm$ in diameter) which cannot be fully visualised owing to the limited resolution of angiography.

An alternative technique, initially described by Sturdy et al. [16], modelled the wall of the vessel as a porous boundary through which side branch flow would virtually 'leak'. Here, the magnitude of leak was determined by taper of the main vessel, which was used to infer the size and flow loss of unsegmented side branches according to Murray's law [17] of vascular scaling:

$$Q \propto D^c, \tag{1}$$

Where D represents artery diameter, Q absolute flow and c the flow diameter exponent, which was originally described by Murray as 3.0 [17]. This first model assumed a homogenous distribution of side branches, with reducing

leakage along the vessel length [18]. Further work regionalised leakage to bifurcation sites [19] and incorporated simulated local vessel pressure, P, into leakage [13]. However, the true value of the flow diameter scaling exponent has been disputed, with theoretical [20] and observational studies [21] suggesting an exponent closer to 7/3 (2.33). This lower scaling exponent implies relatively smaller side branches, with higher terminal resistance, and therefore less side branch flow. The effect of this discrepancy in exponent value for vFFR [22, 18], absolute flow and CMR is uncertain.

An established thread of research aims to accelerate computation, by reducing the Navier-Stokes equations and coronary geometries to a one dimensional (1D) formulation [23, 24, 25, 26, 27]. Such 1D models have been applied throughout the vasculature. Colebank et al., examined their utility in the pulmonary circulation [28] including physiological and pathophysiological states (chronic thromboembolic pulmonary hypertension) [29]. In the systemic circulation [30], the most significant prior art relates the coronaries (coupling to multi-scale models [31]), to ventricular dysfunction [32] and a description of the complete coronary tree [33]. All the work cited above relies on a 1D formulation in which no vessel leak occurs. However, a need (compelling in the case of the coronaries) to incorporate side branch flow erodes the mathematical foundations of 1D theory, which has not been updated consistently to account for the convective acceleration effects of side branch losses and the logical necessity of boundary slip- to exit the domain, there must be motion at the boundary. While preliminary work suggests that existing approximations may describe vFFR [18, 34], flow and CMR are inherently more sensitive to boundary conditions, which may result in increased error [35]. Global sensitivity analysis (GSA) quantifies the sensitivity of model outputs relative to input uncertainty and is therefore well-suited to expose the significance of these omissions. Previous coronary GSA has focused on vFFR and concluded model geometry i.e. stenosis severity, [36, 37, 38] and outlet boundary resistance [37, 39] dominate output uncertainty. But these authors treat the full range of vFFR$\in [0, 1]$ and do not scrutinise sub-ranges where clinical decision support is particularly useful for vFFR. Considering the FFR diagnostic threshold of 0.80, the "grey zone" of vFFR$\in [0.75, 0.85]$ is critical. This influence of anatomical and flow parameters in clinically important sub-ranges is, to our knowledge, unexplored. In redress, we proceed as follows:

1. Advance the 1D formulation of the Navier-Stokes equations in a tapering geometry, self-consistently to incorporate convective acceleration, the effects of side branch flow, and a necessary boundary slip.
2. To gain insight into the expected difference in vFFR computation, we compare the model in (2) with a previously validated, 1D pre-cursor [18].
3. We then use the novel model to perform the first *output constrained* GSA. The aim of this was to determine input parameter influence upon decomposed sub-domains of vFFR and distal coronary flow, with the intention of identifying influential parameters (i.e., future areas for model development) in the most clinically relevant cases.

## 2. Methods

In this section we describe a 1D model accounting for vessel taper, boundary slip and convective acceleration and then its GSA. See figure 1 for a schematic of our workflow.

### *2.1. Patient recruitment, clinical data collection and vessel segmentation*

Data were sourced from the University of Sheffield coronary physiology repository. This included data from adult patients undergoing clinically indicated cardiac catheterisation for assessment of chronic coronary syndromes at Sheffield Teaching Hospitals NHS Foundation Trust. Data collection for research purposes was approved by Regional Ethics Committees and all patients gave informed consent. A full description of patient recruitment [40], vessel segmentation and simulation workflow has already been reported [10, 19]. In brief, for vessel reconstructions, two angiographic projections of the vessel of interest, acquired $\geq 30$ apart and during end-diastole were manually selected. Table movement between consecutive image acquisitions was manually performed. Vessel contrast gradient was used to semi-automatically trace the vessel centreline and borders with manual correction if required. Finally, a rigid, 3D, axisymmetric geometry was automatically created based on epipolar geometry. To adapt 3D arterial structures into a 1D description, we follow established methods [34, 36]. 3D volume meshes were collapsed to circular cross-sectional areas, $A_i$, with surface normals which were tangent to the vessel centreline, to which the streamwise coordinate was parallel. Spacing between centreline nodes did not exceed 0.5 mm. From each $A_i$ we calculated a local vessel radius $r_i = \sqrt{\frac{A_i}{\pi}}$, the streamwise location of each

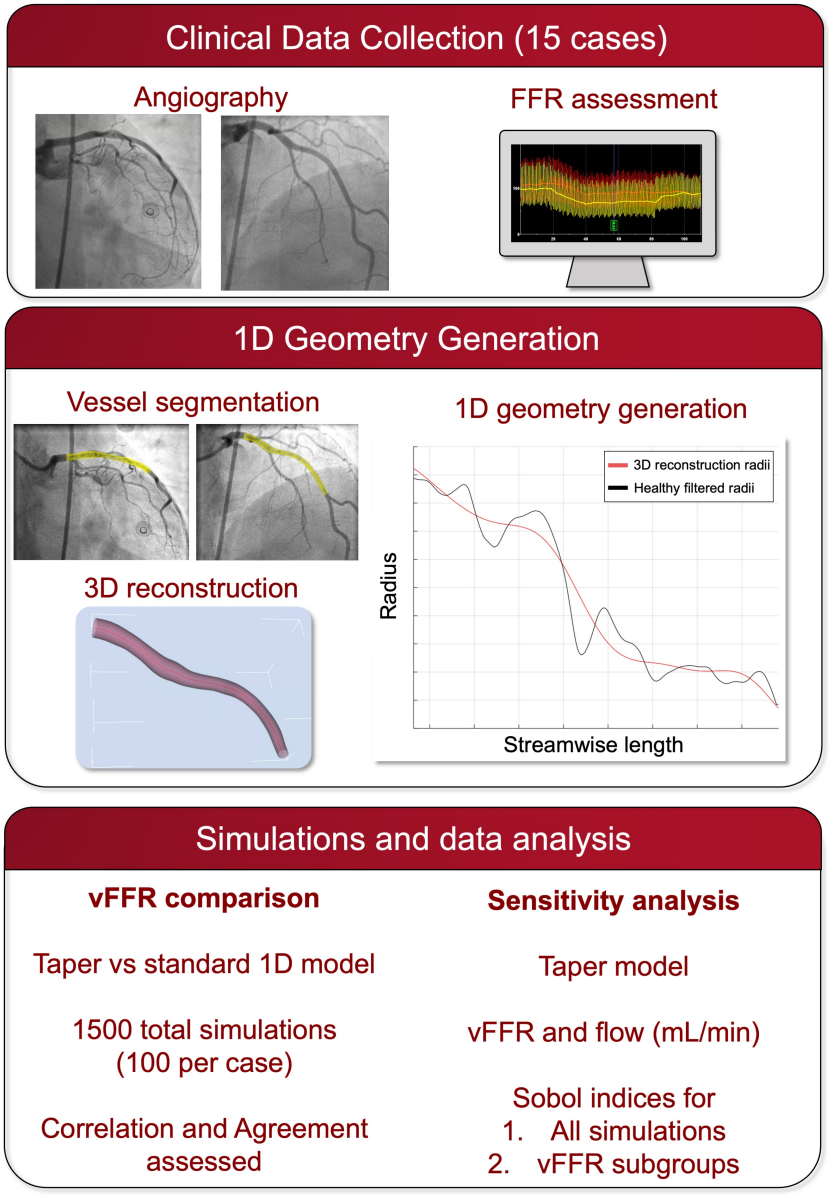


Figure 1: **Schematic representation of the methodology and analysis protocol** Top panel: Clinical Data Collection, patients underwent clinically indicated angiography and FFR assessment (15 total vessels). Middle panel: 1D Geometry Generation, each vessel was manually segmented and 3D reconstruction generated using an epipolar line method. Radius data were then extracted from the 3D reconstruction and Fourier filtration used to model vessel radii as a monotonically decreasing function. Bottom panel: Simulations and data analysis, each Fourier filtered vessel formed a base case onto which artificial stenoses were inserted. Agreement was assessed for taper and standard 1D model-derived vFFR in 1500 artificially stenosed vessels. Sensitivity analyses was then performed, using the taper model, for outputs vFFR and absolute distal flow (mL/min). Sobol indices are presented across all simulations and in distinct vFFR strata.

such segment being computed by summing the Euclidean distance between adjacent centreline points. Thus, the streamwise coordinate of $A_i$, $x_i$, was accumulated as $x_i = \sum_{n=1}^{i} \Delta S_{n-1,n}$. Here, $S_{n-1,n}$ is the Euclidean distance between centreline points indexed $n-1$ and $n$.

*2.2. Idealised vessel construction*

The GSA methodology required suitable 1D representations of healthy vessels (geometries), with an associated inlet flow boundary condition, onto which focal stenoses could be introduced. Idealised geometries are described in section 3.1 and figure 1. To create 1D geometries, radius was sampled at 200 points along the reconstructed centre-line. To filter stenoses from these 1D descriptions, a Fourier filtration was used to transform vessel radius into a monotonically decreasing function of centre-line distance. See Appendix B, in which the black (red) line shows the observed vessel structure (filtered vessel of our synthetic healthy approximation). The Fourier filtration method transforms the centreline-based radius measurements into the frequency domain, suppresses the high-frequency components associated with pathological narrowings, and reconstructs a smoothed radius profile by Fourier inversion, removing focal stenoses while preserving the natural tapering arterial characteristics. This allowed a controlled re-introduction of parameterised stenoses, for our subsequent haemodynamic analyses.

A three step process was used to compute inlet flow in the absence of epicardial stenoses (i.e., healthy inlet flow): a 3D CFD simulation in the original diseased case was first performed, yielding absolute flow at the diseased vessel outlet [5]. Outlet flow in the absence of focal epicardial stenoses was then computed using

$$\text{Healthy outlet flow} = \frac{\text{Diseased outlet flow}}{FFR}.$$

From the above, taper of the artery was used to quantify healthy inlet flow, using the Huo-Kassab flow diameter scaling exponent of 7/3 [20], and our geometrical leak model [13, 36] as follows :

$$\text{Healthy inlet flow} = \text{Healthy outlet flow} \left( \frac{R_{in}}{R_{out}} \right)^{7/3}$$

Here, $R_{in}$ ($R_{out}$) is the vessel inlet (outlet) radius.

*2.3. Haemodynamic descriptions*

*2.3.1. Flow in healthy vessel sections*

A 1D model of steady flow [13], was used to compute vessel flow rate ($Q(x)$ and pressure $P(x)$) in leaky sections of a healthy vessel. The computational domain was a 1D representation of coronary arterial segments, with each vessel parameterised by its centreline (streamwise) coordinate $x \in [0, L]$, with $L$ denoting the total vessel length. The vessel geometry was characterised by a cross-sectional area $A(x) = \pi R^2(x)$, where $R(x)$ is a filtered radius, obtained as described above. Domain boundaries exist at the inlet ($x = 0$) and outlet ($x = L$), with prescribed pressure and flow conditions at the inlet. We adopt a constitutive equation relating pressure and cross-sectional area via a linear wall model [41], applied under the assumptions that the vessel segments are locally cylindrical and the walls are thin, incompressible, homogeneous, and orthotropic. We assume loading and deformation are axisymmetric and that the vessels are tethered in the longitudinal direction.

In this work, $x$ (rather than traditional $z$) denotes the stream-wise co-ordinate, to be consistent with a majority of the relevant literature. Input data were patient-specific: (i) inlet pressure $P_{p,0}$, inlet flow rate $Q_{p,0}$ and (ii) filtered, discretised vessel radii $\{(x_i, R_i); i = 1, .., 200\}$. In Appendix A, we derive the novel 1D initial value problem

$$\begin{aligned}
&\frac{dQ}{dx} + \psi = 0, \\
&\chi \frac{d}{dx}\Big(\frac{Q^2}{A}\Big) + \frac{A}{\rho}\frac{dP}{dx} + \frac{2(\zeta+2)\pi\mu}{\rho}\frac{Q}{A}\left(1 + \Big(\frac{dR}{dx}\Big)^2\right)^{-1/2} + \alpha\frac{Q}{A}\psi = 0, \qquad (2)\\
&Q(0) = Q_{p,0}, \\
&P(0) = P_{p,0}.
\end{aligned}$$

Above, $\alpha$ is a slip parameter, which we formally associate with a notional luminal surface roughness, arising as a consequence of side branch flow. In the base 1D formulation [26, 23], $\frac{dR}{dx} = 0$ is assumed. The assumption of no taper is appropriate for larger systemic vessels [26, 42]. However, in the coronaries, taper is an essential anatomical feature (here ingested through the geometrical data) which, following Appendix A, is included in our 1D formulation. Blood viscosity, $\mu = 0.0035 Pa\ s$, blood density $\rho = 1050 kg/m^3$, flow sink $\psi(x)$ describes local leak (see below), $A(x) = \pi R(x)^2$ is local vessel area, $\zeta$ parameterises transverse variation in stream-wise velocity [43] as

below:

$$u(x,r) = \frac{Q}{A}\left(\frac{\zeta+2}{\zeta}\right)\left[1-\left(\frac{r}{R(x)}\right)^{\zeta}\right], \quad 0 \le r \le R(x), \quad \zeta \in \mathbb{R}^{+}, \tag{3}$$

$\chi$ is a momentum correction coefficient [26]

$$\chi = \frac{A}{Q^2}\iint_A u^2 dA = \frac{\zeta+2}{\zeta+1}, \tag{4}$$

We assume an anatomical model of vessel leak [13] based upon Murray's law. Accordingly, $Q(x)$ and $\psi(x)$ are determined by $R(x)$ (or, equivalently, $A(x)$), given $Q(0)$. The following equation describes the local leak at each vessel segment $x_i$:

$$Q(x) = Q(0)\Big(\frac{A(x)}{A(0)}\Big)^{\frac{c}{2}}, \quad \psi(x) = -\frac{c}{2}\frac{Q(x)}{A(x)}\frac{dA}{dx}. \tag{5}$$

Above, $c$ denotes the Murray exponent. To determine $P(x)$, a numerical scheme was devised using Equations (2) and (5) and a trapezoidal quadrature. Thus, for $\{P(x_i) : i = 1, .., 200\}$

$$\begin{aligned} P(x_{i+1}) = P(x_i) - \rho\left[\frac{2\chi(c-1)-\alpha c}{2(c-2)}\right]\left(\frac{Q(x_{i+1})^2}{A(x_{i+1})^2} - \frac{Q(x_i)^2}{A(x_i)^2}\right) \\ -2(\zeta+2)\pi\mu\int_{x_i}^{x_{i+1}} \frac{Q}{A^2}\left(1+\frac{1}{4\pi A}\Big(\frac{dA}{dx}\Big)^2\right)^{-1/2} dx, \end{aligned} \tag{6}$$

where $Q(x_i)$ is computed from Equation (5), $A(x_i) = \pi R_i^2$ and, in the integrand, $Q$ and $A$ vary linearly over $x_i \le x \le x_{i+1}$. Put another way, each vessel is discretised into 200 segments, derived directly from the reconstructed anatomy, which approximate a conical frustrum with a unique linear taper. These precautions account for vessel taper in the inertial and viscous terms of the momentum equation, while accommodating a boundary momentum flux egress. See Appendix A.

*2.3.2. Flow in stenosed vessel sections*

Abrupt stenotic changes in $R(x)$ involve significant radial flow, invalidating the 1D haemodynamics. A lumped sub-model of, essentially, a Bernoulli resistor can represent flow within the stenosis [44, 45]:

$$\Delta P = AQ + BQ|Q|, \quad A = \frac{K_v\mu}{A_0 D_0}, \quad B = \frac{K_t\rho}{2A_0^2}\left(\frac{A_0}{A_s}-1\right). \tag{7}$$

Above, $A_0$ and $A_s$ are the cross-sectional areas of the healthy and stenotic segments, respectively, $D_0$ and $D_s$ are the healthy and stenotic vessel diameters and $K_v$ and $K_t$ are dimensionless empirical constants quantifying viscous and turbulent effects respectively:

$$K_v = \frac{(K_{v_1} S_c + K_{v_2} D_s)}{D_0} \left(\frac{A_0}{A_s}\right)^2, \; K_{v_1} = 26.56, \; K_{v_2} = 52.48, \; K_t = 1.52,$$

and $S_c$ is the length of the stenosis. Here $\dot{Q} = 0$ thus this term is dropped which is present in previous work. No leak was assumed to occur in stenosed sections of vessels.

*2.4. Diseased geometry generation and boundary condition modulation*

To conduct GSA, synthetic stenoses were inserted into the idealised geometries described in section 2.2. Stenoses were parameterised by:

$$S_s \in [0.1, 0.9], \; S_x \in [0.1, 0.9], \; S_l \in [3.0, 15.0]. \tag{8}$$

Above, $S_s, S_x$ and $S_l$ respectively denote proportional limits for total stenosis luminal area occlusion, location of stenosis centre relative to total vessel length and stenosis length in mm. For example, a stenosis with $S_s = 0.7$ produces a 70% reduction in luminal area at the narrowest point, while $S_x = 0.5$ places it halfway along the vessel length. Parameter $S_l$ controls the length of the stenosis e.g., $S_l = 15.0$, is a 15mm stenosis in the vessel. This approach facilitates the spectrum of clinically representative stenoses, from mild, diffuse narrowings to severe, focal lesions. In all cases, the value of patient-specific invasive proximal flow was modulated in accord with the induced vFFR [13], to provide the inlet flow boundary condition, $Q(0)$.

*2.5. Global sensitivity analysis*

The model above has an input parameter set

$$\{\theta\} = \{S_s, S_x, S_l, c, \zeta, \alpha, K_t, K_{v_1}, K_{v_2}\}. \tag{9}$$

In the variance based methodology of Sobol [46], the first order sensitivity index $S_{1,i} = \mathrm{var}_{\theta_i}.(E_{\theta_i^*}(Y|\theta_i))$, where $\theta_i^* = \{\theta\} \setminus \{\theta_i\}$, subscript $i$ represents the $i$th input parameter and superscript $c$ represents the complementary set of the $i$th parameter. Here, $E$ is the expectation operator and var the variance. Total order estimators, after Homma [47], were computed using

$$S_{T,i} = E_{\theta_i^*}(\mathrm{var}_{\theta_i}(Y|\theta_i^*)) = \mathrm{var}(Y) - \mathrm{var}_{\theta_i^*}(E_{\theta_i}(Y|\theta_i^*)). \tag{10}$$

Above, $S_{T,i}$ quantifies the total effect, of input parameter $\theta_i$

$$S_{T,i} = S_{1,i} + \sum_{i \neq j} S_{ij} + \sum_{i \neq j \neq k} S_{ijk} + ..., \tag{11}$$

Re-arranging $S_{T,i} - S_{1,i} = \sum_{i \neq j} S_{ij} + \sum_{i \neq j \neq k} S_{ijk} + ... = S_{H,i}$, where $S_{H,i}$ denotes the higher order interactions, for an input parameter $\theta_i$. $S_{H,i} \to 0$ implies that model input parameter $\theta_i$ impacts the studied output independently of $\theta_i^*$. In this case, $S_{T,i}$ is a proxy of $S_{1,i}$ as the model parameter effects can be considered independent.

Table 1 declares the assumed bounds of our model input parameters. Ranges align with published theoretical and experimental observations and are tailored to the interval of clinical interest, for revascularisation [21]. GSA is used to analyse both the global impact of input parameters and their effects in the following output vFFR strata which reflect CAD stratification:

(1) vFFR $\in [0.00, 1.00]$, (2) vFFR $\in [0.95, 1.00]$, (3) vFFR $\in [0.85, 0.95]$,
(4) vFFR $\in [0.75, 0.85]$, (5) vFFR $\in [0.65, 0.75]$, (6) vFFR $\in [0.00, 0.65]$.

So, we perform conventional GSA, while binning model outputs into the above intervals. Region (4) is termed the grey zone, in which correctly predicting physiological lesion significance, and therefore recommending revascularisation, is most difficult (the diagnostic threshold for FFR is $\leq 0.80$). Our GSA exposes the variation of input parameter effects within such grey regions.

To compute the sensitivity indices, two $n \times m$ sample matrices $A, B$ were generated. $n$ is the sample number and $m$ the input space dimension. $A, B$ were then used with a variance estimator, to calculate input effects [48, 49]. A & B contain the parameter vectors which produces output- in this case, vFFR and Q. To sample the input parameter sufficiently, we utilised the low discrepancy Sobol sequence, to optimise sensitivity indices' convergence and parameter independence statistical properties. For certain parameter vectors, vFFR will not satisfy the criteria (1)-(6) above, so a modified total order estimator was used

$$S_{T,i} = \sum_{i}^{n-N} \frac{[f(A) - f(A_B^i)]^2}{2(n-N)}. \tag{12}$$

Above, $f$ denotes the solution to the model, $A_B^i$ is a sample matrix constructed from our $A$ and $B$, in which all the rows are from $A$ except the $i$-th, which is extracted from $B$, and $N$ is the number of sample points which failed to produce output within range. For this work, $n = 1,000,000$ sample points were used for each geometry and resampling with replacement was used 1000 times to ensure index convergence. To obtain an average sensitivity, sensitivity estimates were averaged across all 15 geometries. Please see figure 1 for a schematic representation of the methods and analysis protocol. It is important to acknowledge the number of simulations which are required in order to perform this analysis. For a full GSA with first and total order effects, one should perform $n(|p| + 2)$ model executions [50], where $n$ is the number of samples and $|p|$ is the dimensionality of the input space. Here, $|p| = 9$, so to produce outputs for 1 geometry, we require $1,000,000(9 + 2) = 11,000,000$ model executions; so for our 15 geometries, we require $15 \times 11,000,000 = 165,000,000$ model executions in total. Then, from the outputs we can stratify the results; in these strata, sensitivity indices are calculated. As we are only examining single vessels in this work, we can calculate the model outputs directly. However, for more computationally expensive tasks surrogate models have are effective for performing 1D model GSA [51].

| Parameter | Description | Base Value | Bounds | Source |
|---|---|---|---|---|
| $S_s$ | Stenosis Severity | 0.35 | [0.1, 0.9] | [52, 53] |
| $S_x$ | Stenosis Position | 0.5 | [0.1, 0.9] | [52] |
| $S_l$ | Stenosis Length | 7.0 | [3.0, 15.0] | [52] |
| $c$ | Flow Diameter Exponent | 2.33 | (2.0, 3.0] | [36, 17, 20, 54] |
| $\zeta$ | Flow Velocity Exponent | 4.31 | [1.0, 9.0] | [26, 43] |
| $\alpha$ | Surface Roughness | 0.7 | [0.4, 1.0] | [55] |
| $K_t$ | Stenotic Turbulant Coefficient | 1.52 | [1.064, 1.976] | [45, 56] |
| $K_{v_1}$ | Stenotic Viscous Coefficent | 26.56 | [18.592, 34.528] | [45, 56] |
| $K_{v_2}$ | Stenotic Viscous Coefficent | 52.48 | [36.736, 68.224] | [45, 56] |

Table 1: **GSA Parameter bounds:** The input parameters which are utilised within our model and their respective lower and upper bounds for the GSA.

### *2.6. Statistical Analysis*

Categorical variables (i.e., dichotomised vFFR lesion significance) are presented as frequency (percentage). The Shapiro–Wilk test was used to assess

the spread of data. Normally distributed continuous variables are presented as mean (± standard deviation), while skewed data are presented as median [inter-quartile range]. Correlation was quantified using Pearson's correlation coefficient (r). Agreement was assessed with Passing and Bablok regression and quantile regression Bland Altman plots.

## 3. Results

### *3.1. Patient characteristics*

Fifteen coronary arteries, from nine patients were included. Vessels were selected to encompass the range of clinically relevant anatomical variation which may be encountered in routine practice and included seven left anterior descending (LAD), two left circumflex (LCx), four right coronary arteries (RCA), one diagonal branch and one obtuse marginal branch. The observed and synthetic healthy vessels are shown in Appendix B. These synthetic vessels can then be used to evaluate various scenarios, e.g. comparing the novel and standard model [18] and performing the stratified GSA. Seven patients were male, mean age was 67.4 (± 9.1) years old and four (44%) patients were overweight or obese (BMI > 25). Mean vessel inlet flow was 264 (± 150 /min), and the proportional difference between vessel radius inlet and outlet (i.e., total taper) was 38% (± 15%). See table 2 for full haemodynamic results.

### *3.2. Model Outputs*

The taper model was compared with the standard model of leak ($\frac{dR}{dx} = 0, \chi = 1, \alpha = 0, \Psi = 0$) [18] for vFFR. One-hundred simulations were performed in each of the 15 geometries, with stenoses parameterised within the limits declared in table 1. Of the 1500 simulations, 1314 yielded paired data with vFFR$\in [0, 1]$. Failures were predominantly attributed to edge cases (i.e. at the end of model parameters bounds) which did not produce a geometry amenable to simulation. The mean vFFR was $0.81 \pm 0.006$ for the taper model and $0.80 \pm 0.006$ for the standard model. Correlation between the two models was statistically significant (r = 0.99, p < 0.0001 ). Passing and Bablok regression did not identify significant constant or proportional differences between the methods (m = 0.95, 95% CI 0.80 to 1.17; c = 0.03, 95% -0.19 to 0.20)(figure 2). At the vFFR diagnostic threshold, mean bias was 0.00 with 95% CI [-0.04, 0.06]. There was a trend towards poorer agreement between the models at lower vFFR values. Lesion significance (vFFR $\leq$ 0.80) differed

| Case number | Vessel | Pa | Healthy inlet flow | Inlet radius | Outlet radius |
|---|---|---|---|---|---|
| 1 | LAD | 83 | 366.1 | 1.58 | 0.84 |
| 2 | LCx | 45 | 307.8 | 1.62 | 0.88 |
| 3 | RCA | 79 | 279.0 | 1.81 | 1.25 |
| 4 | LAD | 74 | 464.1 | 1.84 | 1.08 |
| 5 | D1 | 81 | 558.3 | 1.56 | 1.05 |
| 6 | LAD | 52 | 120.0 | 1.82 | 0.98 |
| 7 | LAD | 65 | 222.7 | 1.06 | 0.91 |
| 8 | LCx | 79 | 135.6 | 1.54 | 1.00 |
| 9 | LAD | 84 | 246.8 | 1.69 | 0.53 |
| 10 | RCA | 91 | 433.4 | 1.81 | 0.99 |
| 11 | LAD | 51 | 368.0 | 1.31 | 0.88 |
| 12 | OM1 | 57 | 123.8 | 1.56 | 0.76 |
| 13 | LAD | 86 | 80.1 | 1.26 | 0.73 |
| 14 | RCA | 76 | 77.4 | 1.07 | 0.96 |
| 15 | RCA | 109 | 178.2 | 1.20 | 0.93 |

Table 2: **Summary of vessel characteristics used to define the healthy, reference vessels.** Healthy inlet flows correspond to the artery ostium (i.e., left or right main coronary stem). Vessel type denotes the branch in which the reconstruction terminates. All pressures represent mmHg, flows represent mL/min and radii are mm. D1, First diagonal branch;LAD, Left anterior descending artery; LCx, Left circumflex artery; RCA, Right coronary artery; OM1, First obtuse marginal branch.

in 22 cases (1.7%) between taper and standard models. These 22 discordant cases were evenly split between vFFR positive and negative cases (i.e., the taper model categorised eleven cases as false positives and eleven as false negatives).

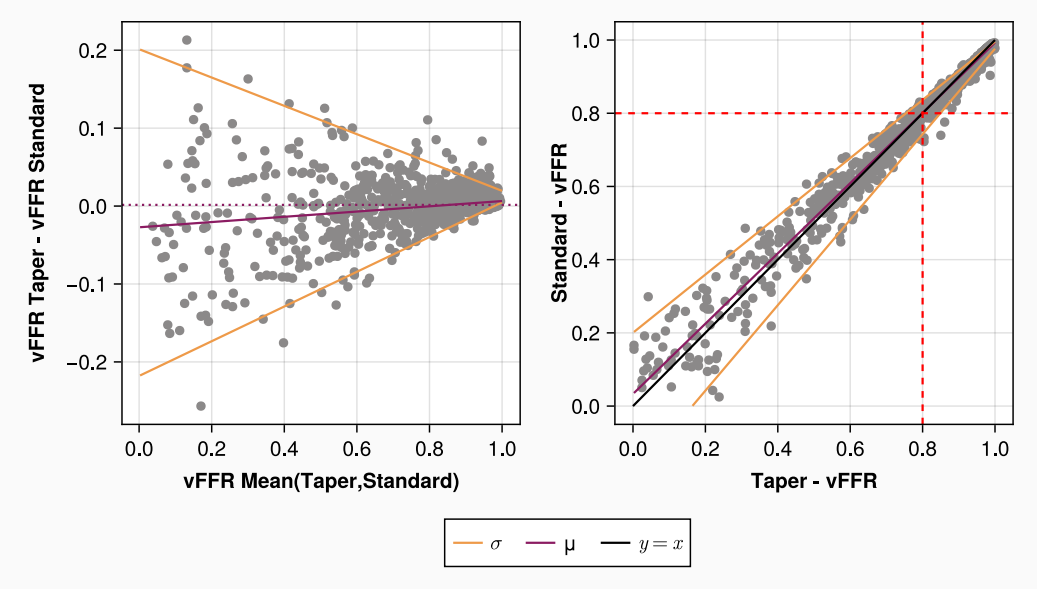


Figure 2: **Quantile regression plot and Passing Bablok plot comparing the two vFFR models** The left figure displays a quantile regression plot comparing the vFFR values for the novel tapering 1D formulation derived in this work against the previously validated 1D model of side branch flow developed by Gosling et al., [18]. The right figure displays a Passing Bablok regression comparing vFFR values obtained from the taper model (x-axis) against the standard 1D formulation including side-branch flow (y-axis).

### *3.3. Global Sensitivity Analysis*

#### *3.3.1. Full Output consideration*

First and total order indices were first calculated for all input parameters in figure 3. Across all simulations, stenosis severity, $S_s$, was most influential on vFFR (first order index ($S_i$) 0.88 $[0.80-0.91]$, total order index ($S_T$) 0.88 $[0.80-0.93]$). Input parameter influence on $Q_d$ was more variable, where the two most influential input parameters were c ($S_1$ 0.33 $[0.15-0.49]$, $S_T$ 0.45 $[0.29-0.55]$) and stenosis position, $S_x$ ($S_1$ 0.30 $[0.08-0.33]$, $S_T$ 0.42 $[0.35-0.60]$). Across all simulations, error of first and total order indices

was less than 0.01 and thus these are not displayed on the box and whisker plot.

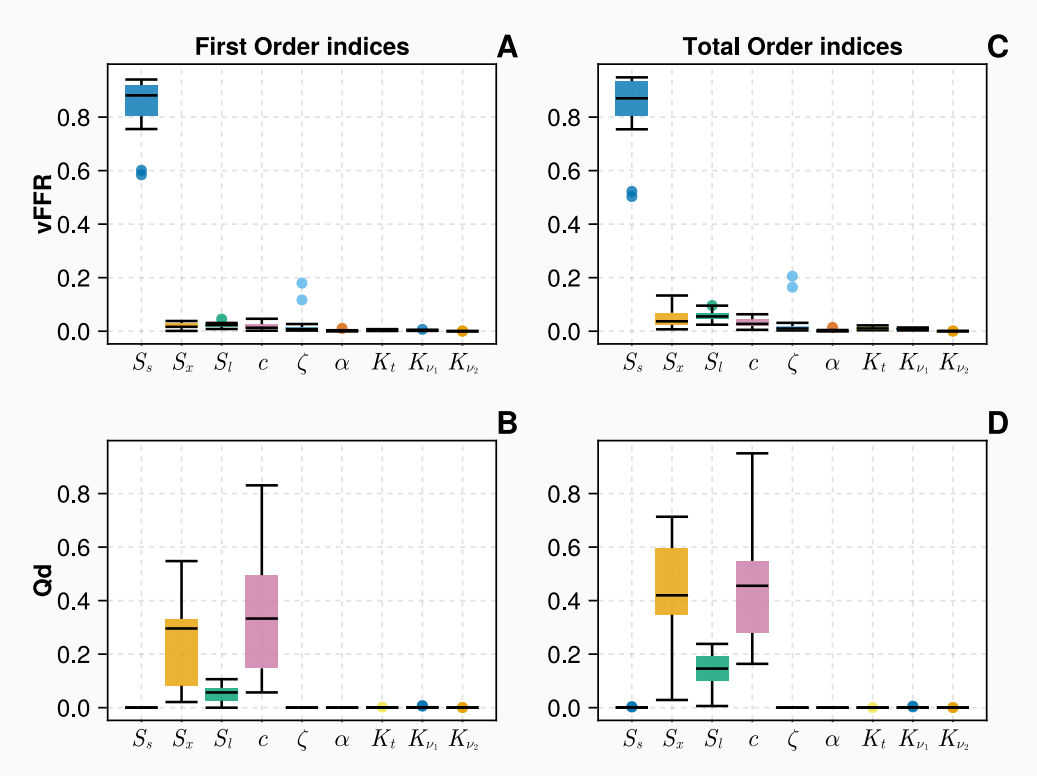


Figure 3: **First and total order indices for vFFR and $Q_d$** The first and total order indices are displayed for the vFFR and $Q_d$. Panes A & B display the independent first order effects for the input parameters of the taper model derived in this work against the outputs vFFR and $Q_d$ respectively. Panes C & D display the total order indices for the same set of input parameters against vFFR and $Q_d$ respectively. The points outside the box and whisker are those which exist more than 1.5 times the IQR which is a end of a whisker. We consider these points to be the outliers.

### *3.3.2. vFFR Stratification*

Total order indices were then computed across distinct vFFR strata detailed in section 2.5 are presented in figure 3. In cases of non flow limiting stenoses (vFFR $\in [0.85, 1.0]$), figure 4A and 4C showed $S_s$ was minimally influential over vFFR, which was instead most sensitive to c, $S_x$, and $S_l$. For intermediate epicardial lesions (vFFR $\in [0.75, 0.85]$), figure 4E showed

vFFR was most sensitive to $S_s$ ($S_T$ 0.26 $[0.24 - 0.30]$), but the input parameters c, $S_x$, and $S_l$ retained comparable influence over vFFR results. In cases of stenoses causing significant flow limitation (vFFR $< 0.75$) as seen in figures 4G and 4I, $S_s$ became increasingly dominant on vFFR results (vFFR $\in [0.65 - 0.75]$, $S_T$ 0.30 $[0.24 - 0.38]$ and vFFR $< 0.65$ $S_T$ 0.38 $[0.32 - 0.44]$). Contrasting with vFFR results, c and $S_x$ were consistently the most influential input parameters on $Q_d$ across the entire spectrum of epicardial disease severity. Figure 4 displays the total order indices for the input parameters against vFFR and $Q_d$. All errors for the total order indices were less than 0.001. Figure 3, shows only very small variations between first and total order indices, therefore, we only display the total order indices here.

## 4. Discussion

In this study, we have described a novel 1D formulation of the Navier-Stokes equations, which incorporates a generalised description of convective acceleration effects of side branch flow and the presence of slip at the luminal boundary. This was implemented in a 1D, leaky vessel model of coronary flow, compared with a previously validated 1D model and we performed a GSA, examining the impact of input parameters on vFFR and $Q_d$.

### *4.1. Comparison with current models of coronary flow*

We conducted an extensive GSA of this taper model, performing 165 million model executions, to analyse the impact of input parameters on vFFR and $Q_d$ both globally and in distinct vFFR strata. As we have derived a direct integration scheme (see equation A.19), a single model evaluation takes 0.00075 seconds which permits extensive model analysis. Previous coronary GSA work has focused on vFFR in non-leaky vessels across the output range 0 to 1. Model geometry, namely stenosis severity, [36, 37, 38], and distal resistance [39] frequently emerge as dominant input parameters and the former is corroborated by our investigation. However, as reconstruction accuracy [57] and models of patient-specific CMR prediction [58] have been validated, the second-order determinants of accuracy are becoming increasingly relevant. By conducting an output-constrained GSA, which analysed mainly intermediate severity stenoses for grey zone vFFR values, we were able to identify these second-order parameters. For the intermediate cases in which vFFR is most clinically useful, this showed the influence of stenosis severity was

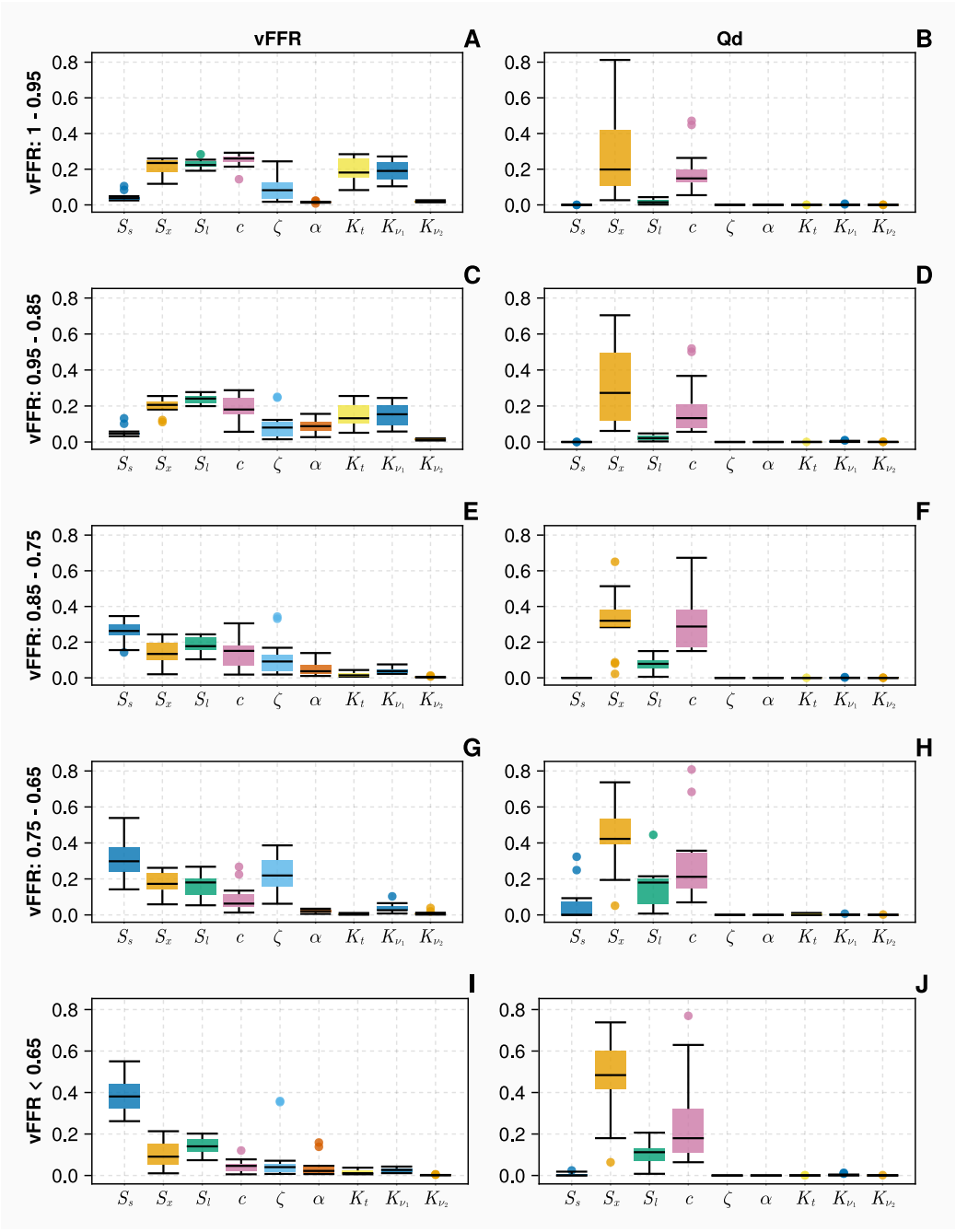


Figure 4: **Total order indices for different vFFR groups:** Panes A,C,E,G,I display total order indices for vFFR results, stratified by the vFFR ranges specified in section 2.5. For these corresponding ranges, the total order indices are displayed for $Q_d$ in panes B,D,F,H,J.

comparable with stenosis location, length and the flow diameter scaling exponent, c. Therefore, when geometries closely resemble true anatomy and patient-specific MVR is reasonably approximated, our results suggest inclusion of side branch flow and the value of the flow diameter exponent used become influential in clinically relevant applications of vFFR. Our investigation included values of c across the theoretical range of 2.0 - 3.0 [17, 20] this range considers both laminar and turbulent, unsteady flow in addition to the rheological properties of blood [54, 59]. A recent meta-analysis derived an optimal exponent of 2.39 [21] and while this may serve as a suitable population average, future work may wish to examine the potential benefit of patient-specific exponent personalisation. Our GSA results also demonstrated the influence of side branch flow across the spectrum of epicardial disease severity when predicting CMR, the importance of which is likely to increase given the heightened recognition of CMD in international guidelines [60]. While outside the present scope, arterial WSS is a known contributor to the progression of stenosis, particularly at side branches. Further investigation into the influence of various wall mechanics models, on vFFR, would provide complementary insight into the influential factors [61].

Previous 1D models of coronary side branch flow did not fully account for resultant fluid convective acceleration or luminal boundary slip and neglected the impact of vessel taper [23, 24, 25, 26, 27]. Implications of these assumptions were uncertain for vFFR accuracy [18, 62]. Our taper model, accounting for these phenomena, was compared with a pre-existing anatomical model of side branch flow in 1314 simulations. The new model was mildly influential on vFFR, suggesting a change in management in 2% of total cases. This is reassuring; previous work has demonstrated negligible mean bias between virtual and invasive FFR [63, 64]. Therefore, this updated methodology may incorporate a more physiologic representation of side branch flow whilst preserving the known diagnostic accuracy of traditional models. An invasive validation will be important to evaluate if these differences translate to improved diagnostic accuracy.

### *4.2. Output Constrained GSA*

The output-constrained GSA methodology presented in this work represents a significant advancement over traditional sensitivity analyses that consider the entire output range. By stratifying results into clinically meaningful ranges (e.g., vFFR grey zone, severe stenosis), we reveal parameter

influences that would otherwise be masked in global analyses. For vFFR values within the grey zone (0.75-0.85), where decisions are most challenging, our results demonstrate that stenosis severity is *not* exclusively dominant, as previously assumed. A more nuanced approach is warranted, based on a combination of anatomical factors including stenosis position, length, and underlying flow distribution patterns, determined by side branch characteristics. The flow diameter scaling exponent emerged as influential in the grey zone, suggesting that accurate modelling of side branch flow could be the difference between intervention and conservative management. This challenges the current clinical paradigm, which emphasises stenosis percentage, and indicates that comprehensive evaluation of coronary anatomy and branch patterns might improve diagnostic accuracy, where it matters most. For such intermediate cases, implementing more sophisticated computational models which account for individualised branching patterns and flow distribution could reduce diagnostic uncertainty and improve patient outcomes.

This approach acknowledges that parameter sensitivity is not uniform across the output space, particularly in physiological systems where clinical decision thresholds create distinct operational regimes. Our findings demonstrate that within the critical vFFR grey zone (0.75-0.85), anatomical parameters and flow scaling exponents exert influence comparable to stenosis severity—a finding obscured in previous whole-range analyses. This methodology could be readily extended to other cardiovascular applications. For instance, applying constrained GSA to ventricular mechanics models could identify critical parameters affecting cardiac output within specific pathophysiological ranges. This approach could isolate which hemodynamic factors most influence plaque vulnerability within specific shear stress ranges associated with rupture risk. By focusing computational resources on regions of clinical uncertainty, output-constrained GSA provides a framework for targeted model refinement where accuracy is most critical for patient outcomes, potentially improving diagnostic specificity across multiple domains of cardiovascular medicine.

### *4.3. Limitations*

Our model used a computationally-derived flow inlet boundary condition which would not be available in routine clinical practice. However, patient-specific CMR may be used as a substitute for vFFR calculations and distal pressure for $Q_d$. The stenosis model is empirically derived and applies the

same mechanical description for each vessel investigated. It therefore considers only concentric lesions [45]. The use of a stenosis model is vital due to the current 1D description assuming negligible radial flow but future work may address this deficiency [65]. We did not formally evaluate the influence of MVR in the vFFR GSA. In reality, the parameters of the model are unlikely to independent, despite our assumptions to the contrary. This work does not consider real-world challenges of clinical applications [66], it is possible failure rate may be higher using values for the flow diameter scaling exponent close to 2.0 due to the (c-2) terms in the denominator. The work considers only single lumen reconstructions of coronary arteries. Effects of the taper model will be less pronounced in right coronary arteries, which typically exhibit fewer branches. The taper model of flow has not been validated against invasive measurements which should be the subject of further work. While the model is able to compute WSS, it does not consider elastic properties of the vessel wall or 3D structure of bifurcations.

## 5. Conclusion

This study describes a novel, 1D formulation of the Navier-Stokes equations, accounting for convective acceleration effects of side branch flow in addition to luminal boundary slip, which are more anatomically consistent with true coronary flow. The novel output constrained GSA showed influence of side branch flow inclusion and accuracy of the flow diameter exponent are highly relevant for grey zone vFFR predictions. When predicting $Q_d$, the flow diameter exponent and stenosis position were universally influential on results. While further validation work is needed, this model represents a refinement of current CFD techniques for predicting coronary flow and highlights the importance of factors other than stenosis severity and microvascular resistance in predicting coronary physiology.

## Appendix A. Numerical Scheme Derivation

The following is based upon the treatment of 1D flow in a tapering artery with leak, due to Hughes and Lubliner [43]. We assume the absence of any body force and will eventually simplify to a steady solution, for constant boundary shape. We use cylindrical polar coordinates to exploit an assumed axial symmetry and a known radius function $R = R(x)$. Notation for boundary regions and the corresponding unit normal vectors is defined in table A.3. In axial symmetry, $\hat{n}_\theta = 0$ everywhere.

| | Boundary Element Location | | | |
|---|---|---|---|---|
| | Inlet | Luminal | Outlet | Section $x$ |
| Unit normal, $\hat{n}$ | $-\hat{e}_x$ | $\frac{(R'\hat{e}_x+\hat{e}_r)}{\sqrt{1+R'^2}}$ | $\hat{e}_x$ | $\hat{e}_x$ |
| Identifier | $\partial\Omega_i$ | $\partial\Omega_l$ | $\partial\Omega_o$ | $\partial\Omega_x$ |

Table A.3: **Boundary notations and unit normal vectors**. $\hat{e}_x$ is the streamwise (artery centre-line) direction. All unit normal's are positive pointing away from the enclosed volume. $R' = \frac{dR}{dx}$ is a known function of streamwise co-ordinate, $x$.

*Appendix A.1. Conservation Relations in the Presence of Leak*

Hughes and Lubliner apply Reynolds' transport theorem to a leaking artery to show that for some arbitrary scalar function $\xi(r, x, t)$ [43]

$$\frac{\partial}{\partial t}A\bar{\xi} + \frac{\partial}{\partial x}A(\bar{\xi u_x}) = \iint_{\partial\Omega_x} \frac{D\xi}{Dt}dA + \oint_{C(x)} \xi(\underline{u} - \underline{v}) \cdot \hat{n}dl. \tag{A.1}$$

Above, $\underline{u}(x)$ and $\underline{v}$(x) denote the fluid and boundary motion, $C(x)$ identifies a contour in the luminal boundary lying within a plane perpendicular to the z-axis (axis of symmetry), $A = \pi R(x)^2$ is the smallest area bounded by $C(x)$ and an overbar denotes a cross-sectional area average:

$$\bar{\xi} = \frac{1}{A}\iint_{\partial\Omega_x} \xi dA. \tag{A.2}$$

*Appendix A.1.1. Fluid Volume Balance*

Following Hughes and Lubliner, set $\xi = 1$ in equation (A.1) to obtain

$$\frac{\partial A}{\partial t} + \frac{\partial}{\partial x}A\bar{u_x} + \psi = 0, \quad \psi = -\oint_{C(x)} w_n dl \tag{A.3}$$

where $w_n = (\underline{u} - \underline{v}) \cdot \hat{n}$ is the relative normal component of the fluid motion, or leak, at the luminal boundary. Sink term $\psi(x)$ represents a volumetric flux per unit length of fluid leaving the domain at streamwise location $z$.

*Appendix A.1.2. Streamwise Momentum Balance*

Again following Hughes and Lubliner, set $\xi = u_x(r, x, t)$ in equation (A.1) from which it is immediate that

$$\frac{\partial}{\partial t}A\bar{u_x} + \frac{\partial}{\partial x}A\bar{u_x^2} + \psi_p = \iint_{\partial\Omega_x} \frac{Du_x}{Dt}dA, \quad \psi_p = -\oint_{C(x)} u_x w_n dl. \tag{A.4}$$

Above, $\psi_p$ is a momentum sink associated with momentum flux at the domain boundary. The material derivative in the above is replaced using an approximate form of the z-component of the curvilinear Navier-Stokes equations [43]:

$$\iint_{\partial\Omega_x} \frac{Du_x}{Dt} dA = -\frac{A}{\rho}\frac{\partial \bar{p}}{\partial x} + \frac{\mu}{\rho} \oint_{C(x)} (\hat{n} \cdot \underline{\nabla})\, u_x dl,$$

Expanding the directional derivative in the integrand and substituting into Equation (A.4), we find

$$\frac{\partial}{\partial t} A\bar{u_x} + \frac{\partial}{\partial x} A\bar{u_x^2} + \frac{A}{\rho}\frac{\partial \bar{p}}{\partial x} + \psi_p = \frac{\mu}{\rho} \oint_{C(x)} \frac{\left(R' \frac{\partial u_x}{\partial x} + \frac{\partial u_x}{\partial r}\right)}{\sqrt{1+R'^2}} dl.$$

We suppose the dominant term in the first integration on the right hand side to be $\frac{\partial u_x}{\partial r}$, and noting that $R'$ is constant on contour $C(x)$, we transpose all terms to the left hand side

$$\frac{\partial}{\partial t} A\bar{u_x} + \frac{\partial}{\partial x} A\bar{u_x^2} + \frac{A}{\rho}\frac{\partial \bar{p}}{\partial x} + \psi_p - \frac{2\pi\mu R(x)}{\rho\sqrt{1+R'^2}} \left[\frac{\partial u_x}{\partial r}\right]_{\partial\Omega_L(x)} = 0. \tag{A.5}$$

Momentum sink term $\psi_p$ will be related to the volume sink term (Equation (A.3)) shortly. Finally, we parameterise the convective acceleration using the momentum correction coefficient, which is implicitly defined as follows

$$\chi \bar{u_x}^2 = \frac{1}{A} \iint_{A(x)} u_x^2 dA. \tag{A.6}$$

Parameter $\chi$ can be evaluated subject to assumptions regarding the transverse variation of the velocity profile. The momentum conservation equation may now be written as follows

$$\frac{\partial}{\partial t} A\bar{u_x} + \frac{\partial}{\partial x} \left(\chi A \bar{u_x}^2\right) + \frac{A}{\rho}\frac{\partial \bar{p}}{\partial x} + \psi_p - \frac{2\pi\mu R(x)}{\rho\sqrt{1+R'^2}} \left[\frac{\partial u_x}{\partial r}\right]_{\partial\Omega_L(x)} = 0. \tag{A.7}$$

We assume the following transverse variation of streamwise velocity within the artery, based upon a no-slip condition at the luminal boundary and a profile blunting controlled by parameter $\zeta$ [43, 36]

$$u_x(x,r) = u(x) \left(\frac{\zeta+2}{\zeta}\right) \left[1 - \left(\frac{r}{R(x)}\right)^{\zeta}\right], \quad 0 \le r \le R(x). \tag{A.8}$$

This profile generates the following results straightforwardly

$$\bar{u}_x = u(x), \quad \chi = \left(\frac{\zeta+2}{\zeta+1}\right), \quad \left[\frac{\partial u_x}{\partial r}\right]_{\partial\Omega_L(x)} = -\frac{\bar{u_x}(\zeta+2)}{R(x)}, \quad \psi_p = 0. \quad \text{(A.9)}$$

The last result follows from Equation (A.4), though a no-slip condition at the boundary intuitively excludes leak. A form of the momentum conservation equation follows from substituting Equations (A.9) into Equation (A.7)

$$\frac{\partial}{\partial t}A\bar{u_x} + \chi\frac{\partial}{\partial x}\left(A\bar{u_x}^2\right) + \frac{A}{\rho}\frac{\partial \bar{p}}{\partial x} + \frac{2\pi\mu(\zeta+2)\bar{u_x}}{\rho\sqrt{1+R'^2}} = 0. \quad \text{(A.10)}$$

Taylor et al. used the above form of momentum conservation to compare models of leak [13]. To advance the momentum conservation equation, explicitly to account for a luminal boundary x-momentum flux, engendered by leak, we hypothesise a rough artery wall, interpreting $R(x)$ as a local mean radius and postulate a non-zero velocity at the wall. Put another way, we assume a mean boundary slip velocity, proportional to $\hat{u}_x$ (but retain Equation A.8)

$$u_x(x, R(x)) = \alpha\hat{u}_x.$$

Above, $\alpha$ is a constant of proportionality parameterising a slip which we formally associate with luminal surface roughness. Of course $\alpha = 1$ corresponds to the plug flow. Accordingly

$$\psi_p(x) = -\oint_{C(x)} u_x w_n dl \to -\alpha\bar{u_x}\oint_{C(x)} w_n dl = \alpha\bar{u_x}\psi(x)$$

Our current form for the momentum conservation equation, which is consistent with Hughes and Lubliner's result [43], now follows

$$\frac{\partial}{\partial t}A\bar{u_x} + \chi\frac{\partial}{\partial x}\left(A\bar{u_x}^2\right) + \frac{A}{\rho}\frac{\partial \bar{p}}{\partial x} + \alpha\bar{u_x}\psi(x) + \frac{2\pi\mu(\zeta+2)\bar{u_x}}{\rho\sqrt{1+R'^2}} = 0. \quad \text{(A.11)}$$

Let us adapt the steady-state conservation Equations A.11 and A.3 in terms of the flow $Q = A\bar{u}_x$ and $\bar{p} = P$ along with the initial conditions for the problem

$$\begin{aligned}
&\frac{dQ}{dx} + \psi = 0,\\
&\chi\frac{d}{dx}\left(\frac{Q^2}{A}\right) + \frac{A}{\rho}\frac{dP}{dx} + K\frac{Q}{A}\left(1+R'^2\right)^{-1/2} + \alpha\frac{Q}{A}\psi = 0, \quad \text{(A.12)}\\
&Q(0) = Q_0,\\
&P(0) = P_0.
\end{aligned}$$

Above, the artery geometry, the function $A(x)$, is a known function, $Q_0$ is a known inlet flow and we have defined

$$K = \frac{2(\zeta+2)\pi\mu}{\rho}.$$

Equations A.12 are supplemented by our assumed model of anatomical leak, based upon Murray's law [17], but with a relaxed exponent, denoted $c$

$$Q(x) = Q(0)\left(\frac{A(x)}{A(0)}\right)^{\frac{c}{2}}, \tag{A.13}$$

which allows us to assign $\psi$

$$\psi = -\frac{dQ}{dx} = -\frac{c}{2}\frac{Q_0}{A(0)^{\frac{c}{2}}}A^{\frac{c}{2}-1}\frac{dA}{dx}, \tag{A.14}$$

and to consider only the second of Equations A.12, in which substitute our expression for $\psi$. After a little straightforward algebra

$$\frac{dP}{dx} + \frac{\rho Q_0^2}{A_0^c}A^{c-3}\frac{dA}{dx}\left(\chi c - \chi - \frac{\alpha c}{2}\right) + \frac{\rho K Q_0 A^{c/2-2}}{A_0^{c/2}}\left(1+R'^2\right)^{-1/2} = 0. \tag{A.15}$$

Note that Equation A.13 allows us directly to assign $Q(x)$, given $A(x)$ and initial condition $Q_0$. Seeking a numerical solution for $P(x)$, we integrate the above between two consecutive streamwise locations $x_i$ and $x_{i+1}$

$$\begin{aligned} P_{i+1} - P_i + \left(\frac{2\chi c - 2\chi - \alpha c}{2c-4}\right)\frac{\rho Q_0^2}{A_0^c}\left(A_{i+1}^{c-2} - A_i^{c-2}\right) \\ + \frac{\rho K Q_0}{A_0^{c/2}}\int_{x_i}^{x_{i+1}} A^{c/2-2}\left(1+R'^2\right)^{-1/2} dx = 0. \end{aligned} \tag{A.16}$$

Finally, a compact and easy to implement numerical scheme results when we substitute for $K$, use Equation A.13 and eliminate $R'$ in favour of $A = \pi R(x)^2$

$$\left(\frac{dR}{dx}\right)^2 = \frac{1}{4\pi A}\left(\frac{dA}{dx}\right)^2. \tag{A.17}$$

Substituting this, write to clearly identify the inertia and viscous terms. All in terms of area and flow.

$$\begin{aligned} P_i - P_{i+1} = \rho\left[\frac{2\chi(c-1) - \alpha c}{2(c-2)}\right]\left(\frac{Q_{i+1}^2}{A_{i+1}^2} - \frac{Q_i^2}{A_i^2}\right) \\ + 2(\zeta+2)\pi\mu\int_{x_i}^{x_{i+1}} \frac{Q}{A^2}\left(1 + \frac{1}{4\pi A}\left(\frac{dA}{dx}\right)^2\right)^{-1/2} dx \end{aligned} \tag{A.18}$$

Applying the trapezoidal rule we obtain a computational scheme of:

$$\begin{aligned}\Delta P_i &= \rho\left[\frac{2\chi(c-1)-\alpha c}{2(c-2)}\right]\left(\frac{Q_{i+1}^2}{A_{i+1}^2}-\frac{Q_i^2}{A_i^2}\right)\\ &+\pi\mu(\zeta+2)\Delta x\left[\frac{Q_{i+1}}{A_{i+1}^2}\left(1+\frac{1}{4\pi A_{i+1}}\left(\frac{A_{i+2}-A_{i+1}}{\Delta x}\right)^2\right)^{-1/2}\right.\\ &\left.+\frac{Q_i}{A_i^2}\left(1+\frac{1}{4\pi A_i}\left(\frac{A_{i+1}-A_i}{\Delta x}\right)^2\right)^{-1/2}\right]\\ P_{i+1} &= P_i-\Delta P_i\end{aligned} \tag{A.19}$$

Where $\Delta x$ is each vessel segment length. This numerical scheme is valid for the healthy parts of the vessel. At a stenosis, to calculate the pressure drop we utilise the methodology in section 2.3.2. By leveraging the assumption that there is no leakage over the stenosis, one must pass the flow rate at position $i$ ($Q_i$) to the lumped model to calculate the pressure drop using equation 7. At the end of the stenosed section, indexed n, the updated flow $Q_n = Q_i$ and pressure $P_n = P_i - \Delta P$ are passed back to the 1D computational scheme above. Here $\Delta P$ is the pressure drop calculated with equation 7.

## Appendix B. Filtered Geometries


## Acknowledgements

HS is supported by the UK Engineering and Physical Sciences Research Council (EPSRC) via grant reference EP/Z531297/1


## Disclosures

No conflicts of interest, financial or otherwise, are declared by the authors

## Author Contributions

H.S, D.J.T, and I.H. conceived and designed research; H.S, D.J.T, R.G, T.N,. and P.D.M,. performed experiments; H.S, D.J.T, I.H, X.X, and A.J.N, analyzed data; H.S. prepared figures; H.S and D.J.T drafted manuscript; K.C, T.N, R.G, D.R.H, L.R.H and J.P.G edited and revised manuscript; All approved final version of manuscript

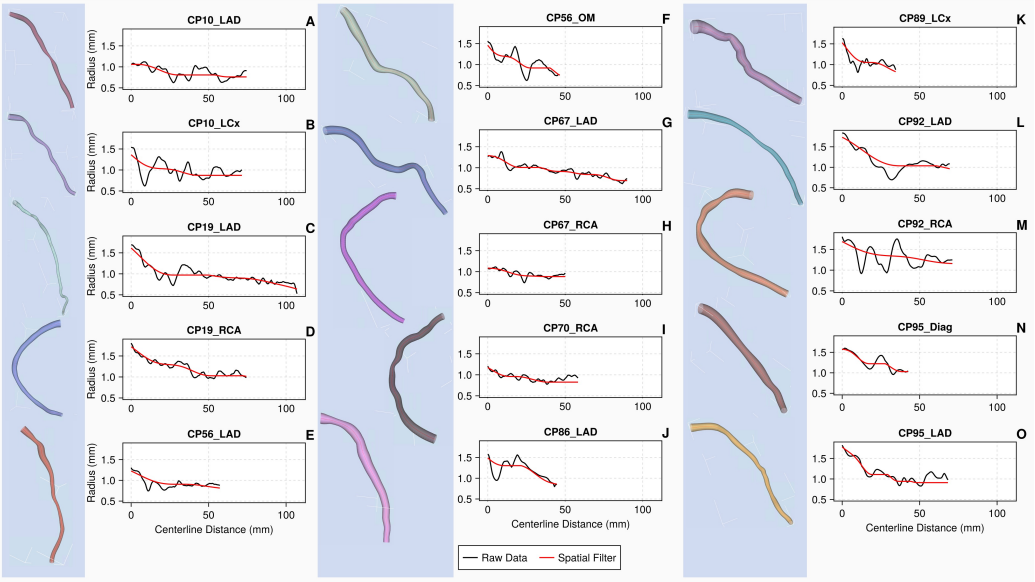


Figure B.5: **3D vessel reconstructions with corresponding segmented (black) and filtered (red) radii**. Each vessel is discretised into 200 segments, derived directly from the reconstructed anatomy, which approximate a conical frustrum with a unique linear taper.

## Data Availability

The data supporting the findings of this study are available from the corresponding author upon reasonable request.

## References


[1] Franz-Josef Neumann, Miguel Sousa-Uva, Anders Ahlsson, Fernando Alfonso, Adrian P Banning, Umberto Benedetto, Robert A Byrne, Jean-Philippe Collet, Volkmar Falk, Stuart J Head, et al. 2018 esc/eacts guidelines on myocardial revascularization. *European heart journal*, 40(2):87–165, 2019.

[2] Pim AL Tonino, Bernard De Bruyne, Nico HJ Pijls, Uwe Siebert, Fumiaki Ikeno, Marcel vant Veer, Volker Klauss, Ganesh Manoharan, Thomas Engstrøm, Keith G Oldroyd, et al. Fractional flow reserve versus angiography for guiding percutaneous coronary intervention. *New England Journal of Medicine*, 360(3):213–224, 2009.

[3] Juhani Knuuti, William Wijns, Antti Saraste, Davide Capodanno, Emanuele Barbato, Christian Funck-Brentano, Eva Prescott, Robert F Storey, Christi Deaton, Thomas Cuisset, et al. 2019 esc guidelines for the diagnosis and management of chronic coronary syndromes: The task force for the diagnosis and management of chronic coronary syndromes of the european society of cardiology (esc). *European heart journal*, 41(3):407–477, 2020.

[4] Ozan M Demir, Coen KM Boerhout, Guus A de Waard, Tim P van de Hoef, Niket Patel, Marcel AM Beijk, Rupert Williams, Haseeb Rahman, Henk Everaars, Rajesh K Kharbanda, et al. Comparison of doppler flow velocity and thermodilution derived indexes of coronary physiology. *Cardiovascular Interventions*, 15(10):1060–1070, 2022.

[5] Paul D Morris, Desmond Ryan, Allison C Morton, Richard Lycett, Patricia V Lawford, D Rodney Hose, and Julian P Gunn. Virtual fractional flow reserve from coronary angiography: modeling the significance of coronary lesions: results from the virtu-1 (virtual fractional flow reserve from coronary angiography) study. *JACC: Cardiovascular Interventions*, 6(2):149–157, 2013.

[6] Charles A Taylor, Timothy A Fonte, and James K Min. Computational fluid dynamics applied to cardiac computed tomography for noninvasive quantification of fractional flow reserve: scientific basis. *Journal of the American College of Cardiology*, 61(22):2233–2241, 2013.

[7] HeartFlow. Heartflow ffrct analysis, 2024. https://www.heartflow.com/heartflow-ffrct-analysis/ [Accessed: (12/6/2024)].

[8] Medis Medical Imaging. Medis qfr®, 2024. https://medisimaging.com/software-solutions/medis-qfr/ [Accessed: (12/6/2024)].

[9] Cathworks. Cathworks ffrangio® system, 2024. https://cath.works/cathworks-ffrangio/ [Accessed: (12/6/2024)].

[10] Paul D Morris, Rebecca Gosling, Iwona Zwierzak, Holli Evans, Louise Aubiniere-Robb, Krzysztof Czechowicz, Paul C Evans, D Rodney Hose, Patricia V Lawford, Andrew J Narracott, et al. A novel method for measuring absolute coronary blood flow and microvascular resistance in patients with ischaemic heart disease. *Cardiovascular research*, 117(6):1567–1577, 2021.

[11] Weihao Li, Kun Lian, Yan Chen, Shuai Zhao, Xiaoqiong Guo, Qian Tao, Haokao Gao, Songyun Xie, Chengxiang Li, Qiong Wang, et al. Computing intracoronary blood flow rate under incomplete boundary conditions: Combing coronary anatomy and fractional flow reserve. *Medical Engineering & Physics*, 111:103942, 2023.

[12] Frank Gijsen, Yuki Katagiri, Peter Barlis, Christos Bourantas, Carlos Collet, Umit Coskun, Joost Daemen, Jouke Dijkstra, Elazer Edelman, Paul Evans, et al. Expert recommendations on the assessment of wall shear stress in human coronary arteries: existing methodologies, technical considerations, and clinical applications. *European heart journal*, 40(41):3421–3433, 2019.

[13] Daniel J Taylor, Harry Saxton, Ian Halliday, Tom Newman, Jeroen Feher, Rebecca Gosling, Andrew J Narracott, Denise van Kemenade, Marcel van't Veer, Pim AL Tonino, et al. Evaluation of models of sequestration flow in coronary arteries—physiology versus anatomy? *Computers in Biology and Medicine*, page 108299, 2024.

[14] Shengxian Tu, Emanuele Barbato, Zsolt Köszegi, Junqing Yang, Zhonghua Sun, Niels R Holm, Balázs Tar, Yingguang Li, Dan Rusinaru, William Wijns, et al. Fractional flow reserve calculation from 3-dimensional quantitative coronary angiography and timi frame count:

a fast computer model to quantify the functional significance of moderately obstructed coronary arteries. *JACC: Cardiovascular Interventions*, 7(7):768–777, 2014.

[15] Peshala T Gamage, Pengfei Dong, Juhwan Lee, Yazan Gharaibeh, Vladislav N Zimin, Hiram G Bezerra, David L Wilson, and Linxia Gu. Fractional flow reserve (ffr) estimation from oct-based cfd simulations: Role of side branches. *Applied Sciences*, 12(11):5573, 2022.

[16] Jacob Sturdy, Johannes Kløve Kjernlie, Hallvard Moian Nydal, Vinzenz G Eck, and Leif R Hellevik. Uncertainty quantification of computational coronary stenosis assessment and model based mitigation of image resolution limitations. *Journal of Computational Science*, 31:137–150, 2019.

[17] Cecil D Murray. The physiological principle of minimum work: I. the vascular system and the cost of blood volume. *Proceedings of the National Academy of Sciences*, 12(3):207–214, 1926.

[18] Rebecca C Gosling, Jacob Sturdy, Paul D Morris, Fredrik Eikeland Fossan, Leif Rune Hellevik, Patricia Lawford, D Rodney Hose, and Julian Gunn. Effect of side branch flow upon physiological indices in coronary artery disease. *Journal of Biomechanics*, 103:109698, 2020.

[19] Daniel J Taylor, Jeroen Feher, Krzysztof Czechowicz, Ian Halliday, DR Hose, Rebecca Gosling, Louise Aubiniere-Robb, Marcel van't Veer, Danielle CJ Keulards, Pim Tonino, et al. Validation of a novel numerical model to predict regionalized blood flow in the coronary arteries. *European Heart Journal-Digital Health*, 4(2):81–89, 2023.

[20] Yunlong Huo and Ghassan S Kassab. A scaling law of vascular volume. *Biophysical journal*, 96(2):347–353, 2009.

[21] Daniel J Taylor, Harry Saxton, Ian Halliday, Tom Newman, DR Hose, Ghassan S Kassab, Julian P Gunn, and Paul D Morris. A systematic review and meta-analysis of murray's law in the coronary arterial circulation. *American Journal of Physiology-Heart and Circulatory Physiology*, 2024.

[22] Dong Yong, Chen Minjie, Zhao Yujie, Wang Jianli, Liu Ze, Li Pengfei, Lai Xiangling, Liu Xiujian, and Del Ser Javier. Diagnostic performance

of ivus-ffr analysis based on generative adversarial network and bifurcation fractal law for assessing myocardial ischemia. *Frontiers in Cardiovascular Medicine*, 10:1155969, 2023.

[23] Alfio Quarteroni, L Formaggia, and A Veneziani. Cardiovascular mathematics. In *Proceedings of the International Congress of Mathematicians*, volume 1, pages 479–512. European Mathematical Society Madrid, Spain, 2006.

[24] Lucas O Müller, Sansuke M Watanabe, Eleuterio F Toro, Raúl A Feijóo, and Pablo J Blanco. An anatomically detailed arterial-venous network model. cerebral and coronary circulation. *Frontiers in Physiology*, 14:1162391, 2023.

[25] Leif Rune Hellevik, Jan Vierendeels, T Kiserud, N Stergiopulos, F Irgens, Erik Dick, K Riemslagh, and Pascal Verdonck. An assessment of ductus venosus tapering and wave transmission from the fetal heart. *Biomechanics and modeling in mechanobiology*, 8:509–517, 2009.

[26] Annemette Sofie Olufsen. Modeling the arterial system with reference to an anesthesia simulator. 1998.

[27] Charles A Taylor, Kersten Petersen, Nan Xiao, Matthew Sinclair, Ying Bai, Sabrina R Lynch, Adam UpdePac, and Michiel Schaap. Patient-specific modeling of blood flow in the coronary arteries. *Computer Methods in Applied Mechanics and Engineering*, 417:116414, 2023.

[28] Mitchel Jonathan Colebank. *Computational modeling of patient specific pulmonary hemodynamics*. North Carolina State University, 2021.

[29] Mitchel J Colebank, M Umar Qureshi, Sudarshan Rajagopal, Richard A Krasuski, and Mette S Olufsen. A multiscale model of vascular function in chronic thromboembolic pulmonary hypertension. *American Journal of Physiology-Heart and Circulatory Physiology*, 321(2):H318–H338, 2021.

[30] Philippe Reymond, Fabrice Merenda, Fabienne Perren, Daniel Rufenacht, and Nikos Stergiopulos. Validation of a one-dimensional model of the systemic arterial tree. *American Journal of Physiology-Heart and Circulatory Physiology*, 297(1):H208–H222, 2009.

[31] Jack Lee and Nicolas P Smith. The multi-scale modelling of coronary blood flow. *Annals of biomedical engineering*, 40:2399–2413, 2012.

[32] Jonathan P Mynard and P Nithiarasu. A 1d arterial blood flow model incorporating ventricular pressure, aortic valve and regional coronary flow using the locally conservative galerkin (lcg) method. *Communications in numerical methods in engineering*, 24(5):367–417, 2008.

[33] Zheng Duanmu, Weiwei Chen, Hao Gao, Xilan Yang, Xiaoyu Luo, and Nicholas A Hill. A one-dimensional hemodynamic model of the coronary arterial tree. *Frontiers in Physiology*, 10:853, 2019.

[34] Pablo Javier Blanco, Carlos Alberto Bulant, Lucas O Müller, GD Maso Talou, C Guedes Bezerra, Pedro A Lemos, and Raúl Antonino Feijóo. Comparison of 1d and 3d models for the estimation of fractional flow reserve. *Scientific reports*, 8(1):17275, 2018.

[35] Lucas O Müller, Fredrik E Fossan, Anders T Bråten, Arve Jørgensen, Rune Wiseth, and Leif R Hellevik. Impact of baseline coronary flow and its distribution on fractional flow reserve prediction. *International journal for numerical methods in biomedical engineering*, 37(11):e3246, 2021.

[36] Fredrik E Fossan, Jacob Sturdy, Lucas O Müller, Andreas Strand, Anders T Bråten, Arve Jørgensen, Rune Wiseth, and Leif R Hellevik. Uncertainty quantification and sensitivity analysis for computational ffr estimation in stable coronary artery disease. *Cardiovascular engineering and technology*, 9:597–622, 2018.

[37] Cyrus Tanade, Bradley Feiger, Madhurima Vardhan, S James Chen, Jane A Leopold, and Amanda Randles. Global sensitivity analysis for clinically validated 1d models of fractional flow reserve. In *2021 43rd Annual International Conference of the IEEE Engineering in Medicine & Biology Society (EMBC)*, pages 4395–4398. IEEE, 2021.

[38] Minglang Yin, Alireza Yazdani, and George Em Karniadakis. One-dimensional modeling of fractional flow reserve in coronary artery disease: Uncertainty quantification and bayesian optimization. *Computer Methods in Applied Mechanics and Engineering*, 353:66–85, 2019.

[39] Paul D Morris, Daniel Alejandro Silva Soto, Jeroen FA Feher, Dan Rafiroiu, Angela Lungu, Susheel Varma, Patricia V Lawford, D Rodney Hose, and Julian P Gunn. Fast virtual fractional flow reserve based upon steady-state computational fluid dynamics analysis: results from the virtu-fast study. *Basic to Translational Science*, 2(4):434–446, 2017.

[40] Louise Aubiniere-Robb, Rebecca Gosling, Daniel J Taylor, Tom Newman, D Rodney Hose, Ian Halliday, Patricia V Lawford, Andrew J Narracott, Julian P Gunn, and Paul D Morris. The complementary value of absolute coronary flow in the assessment of patients with ischaemic heart disease. *Nature cardiovascular research*, 1(7):611–616, 2022.

[41] Soroush Safaei, Christopher P Bradley, Vinod Suresh, Kumar Mithraratne, Alexandre Muller, Harvey Ho, David Ladd, Leif R Hellevik, Stig W Omholt, J Geoffrey Chase, et al. Roadmap for cardiovascular circulation model. *The Journal of physiology*, 594(23):6909–6928, 2016.

[42] Mette S Olufsen, Charles S Peskin, Won Yong Kim, Erik M Pedersen, Ali Nadim, and Jesper Larsen. Numerical simulation and experimental validation of blood flow in arteries with structured-tree outflow conditions. *Annals of biomedical engineering*, 28:1281–1299, 2000.

[43] Thomas JR Hughes and J Lubliner. On the one-dimensional theory of blood flow in the larger vessels. *Mathematical Biosciences*, 18(1-2):161–170, 1973.

[44] Frans N Van de Vosse and Nikos Stergiopulos. Pulse wave propagation in the arterial tree. *Annual Review of Fluid Mechanics*, 43:467–499, 2011.

[45] Donald F Young and Frank Y Tsai. Flow characteristics in models of arterial stenoses—i. steady flow. *Journal of biomechanics*, 6(4):395–410, 1973.

[46] Ilya M Sobol. Global sensitivity indices for nonlinear mathematical models and their monte carlo estimates. *Mathematics and computers in simulation*, 55(1-3):271–280, 2001.

[47] Toshimitsu Homma and Andrea Saltelli. Importance measures in global sensitivity analysis of nonlinear models. *Reliability Engineering & System Safety*, 52(1):1–17, 1996.

[48] Andrea Saltelli, Paola Annoni, Ivano Azzini, Francesca Campolongo, Marco Ratto, and Stefano Tarantola. Variance based sensitivity analysis of model output. design and estimator for the total sensitivity index. *Computer physics communications*, 181(2):259–270, 2010.

[49] Harry Saxton, Xu Xu, Torsten Schenkel, Richard H Clayton, and Ian Halliday. Convergence, sampling and total order estimator effects on parameter orthogonality in global sensitivity analysis. *bioRxiv*, pages 2024–02, 2024.

[50] Andrea Saltelli, Marco Ratto, Terry Andres, Francesca Campolongo, Jessica Cariboni, Debora Gatelli, Michaela Saisana, and Stefano Tarantola. *Global sensitivity analysis: the primer*. John Wiley & Sons, 2008.

[51] MJ Colebank and NC Chesler. Efficient uncertainty quantification in a spatially multiscale model of pulmonary arterial and venous hemodynamics. *Biomechanics and Modeling in Mechanobiology*, pages 1–23, 2024.

[52] Julien Adjedj, Panagiotis Xaplanteris, Gabor Toth, Angela Ferrara, Mariano Pellicano, Giovanni Ciccarelli, Vincent Floré, Emanuele Barbato, and Bernard De Bruyne. Visual and quantitative assessment of coronary stenoses at angiography versus fractional flow reserve: the impact of risk factors. *Circulation: Cardiovascular Imaging*, 10(7):e006243, 2017.

[53] Jonathan Tobis, Babak Azarbal, and Leo Slavin. Assessment of intermediate severity coronary lesions in the catheterization laboratory. *Journal of the American College of Cardiology*, 49(8):839–848, 2007.

[54] Geoffrey B West, James H Brown, and Brian J Enquist. A general model for the origin of allometric scaling laws in biology. *Science*, 276(5309):122–126, 1997.

[55] Kieun Choi, Weiguang Yang, On Shun Pak, and Jongmin Seo. Hemodynamics of slip surfaces for thrombosis control in implanted cardiovascular devices. *Physics of Fluids*, 37(2), 2025.

[56] Donald F Young and Frank Y Tsai. Flow characteristics in models of arterial stenoses—ii. unsteady flow. *Journal of biomechanics*, 6(5):547–559, 1973.

[57] Roshni Solanki, Rebecca Gosling, Vignesh Rammohan, Giulia Pederzani, Pankaj Garg, James Heppenstall, D Rodney Hose, Patricia V Lawford, Andrew J Narracott, John Fenner, et al. The importance of three dimensional coronary artery reconstruction accuracy when computing virtual fractional flow reserve from invasive angiography. *Scientific reports*, 11(1):19694, 2021.

[58] Rebecca C Gosling, Eleanor Gunn, Hua Liang Wei, Yuanlin Gu, Vignesh Rammohan, Timothy Hughes, David Rodney Hose, Patricia V Lawford, Julian P Gunn, and Paul D Morris. Incorporating clinical parameters to improve the accuracy of angiography-derived computed fractional flow reserve. *European Heart Journal-Digital Health*, 3(3):481–488, 2022.

[59] Rémi Revellin, François Rousset, David Baud, and Jocelyn Bonjour. Extension of murray's law using a non-newtonian model of blood flow. *Theoretical Biology and Medical Modelling*, 6:1–9, 2009.

[60] Christiaan Vrints, Felicita Andreotti, Konstantinos C Koskinas, Xavier Rossello, Marianna Adamo, James Ainslie, Adrian Paul Banning, Andrzej Budaj, Ronny R Buechel, Giovanni Alfonso Chiariello, et al. 2024 esc guidelines for the management of chronic coronary syndromes: developed by the task force for the management of chronic coronary syndromes of the european society of cardiology (esc) endorsed by the european association for cardio-thoracic surgery (eacts). *European heart journal*, 45(36):3415–3537, 2024.

[61] Pablo J Blanco and Lucas O Müller. One-dimensional blood flow modeling in the cardiovascular system. from the conventional physiological setting to real-life hemodynamics. *International Journal for Numerical Methods in Biomedical Engineering*, 41(3):e70020, 2025.

[62] Na Li, Bao Li, Yili Feng, Junling Ma, Liyuan Zhang, Jian Liu, and Youjun Liu. Impact of coronary bifurcated vessels flow-diameter scaling laws on fractional flow reserve based on computed tomography images (ffrct). *Mathematical Biosciences and Engineering*, 19(3):3127–3146, 2022.

[63] Guy Witberg, Bernard De Bruyne, William F Fearon, Stephan Achenbach, Thomas Engstrom, Hitoshi Matsuo, and Ran Kornowski. Diagnostic performance of angiogram-derived fractional flow reserve: a pooled

analysis of 5 prospective cohort studies. *Cardiovascular Interventions*, 13(4):488–497, 2020.

[64] Thomas I Faulder, Kurundeniya Prematunga, Soniah B Moloi, Lauren E Faulder, Rhondda Jones, and Joseph V Moxon. Agreement of fractional flow reserve estimated by computed tomography with invasively measured fractional flow reserve: A systematic review and meta-analysis. *Journal of the American Heart Association*, page e034552, 2024.

[65] Suncica Canic, Shihan Guo, Yifan Wang, Xiaohe Yue, and Haibiao Zheng. Extended one-dimensional reduced model for blood flow within a stenotic artery. *arXiv preprint arXiv:2409.16262*, 2024.

[66] Mina Ghobrial, Hazel Haley, Rebecca Gosling, Daniel James Taylor, James Richardson, Kenneth Morgan, David Barmby, Javaid Iqbal, Arvindra Krishnamurthy, Rajender Singh, et al. Modelled impact of virtual fractional flow reserve in patients undergoing coronary angiography (virtu-4). *Heart*, 2024.

# Clinical Data Collection (15 cases)

## Angiography

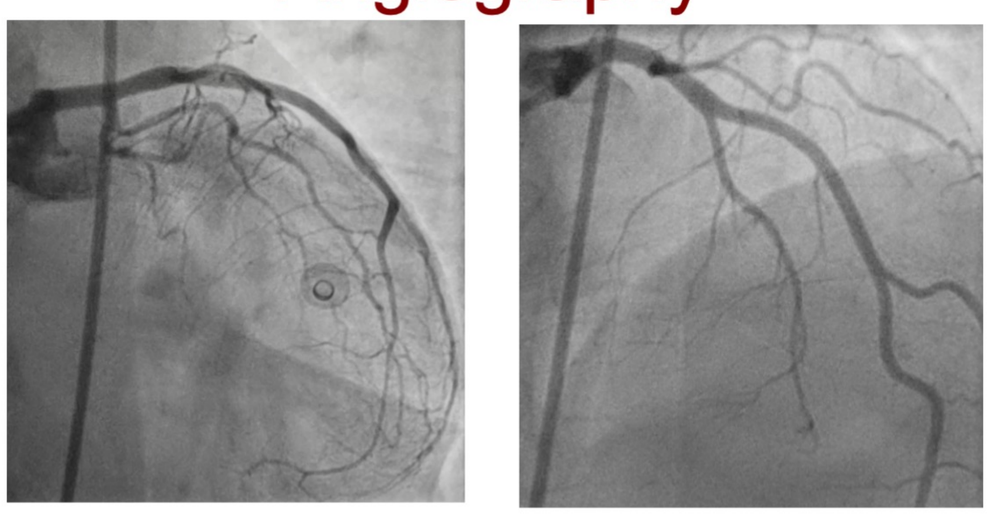

## FFR assessment

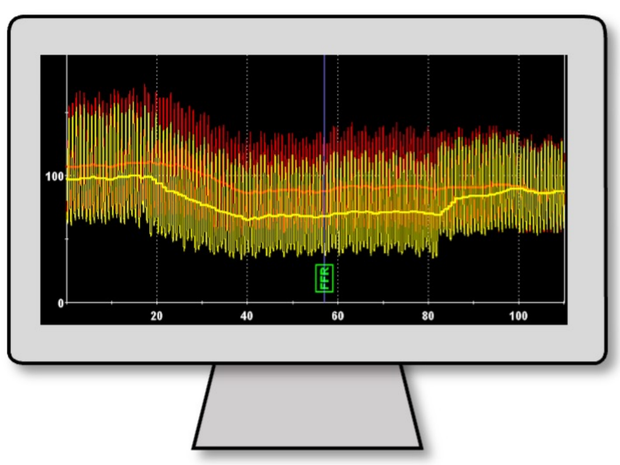


# 1D Geometry Generation

## Vessel segmentation

## 3D reconstruction

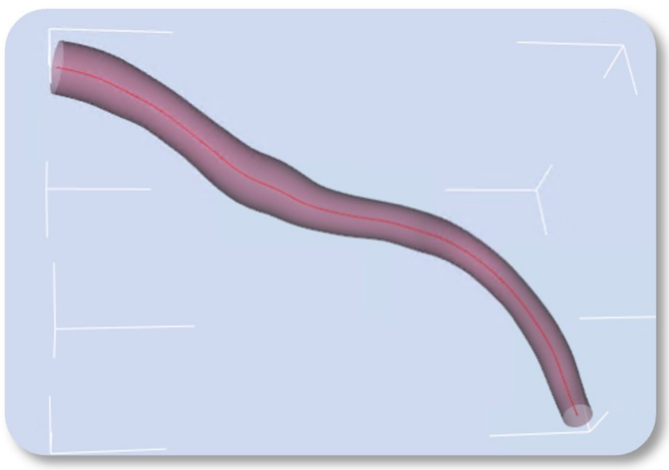

## 1D geometry generation

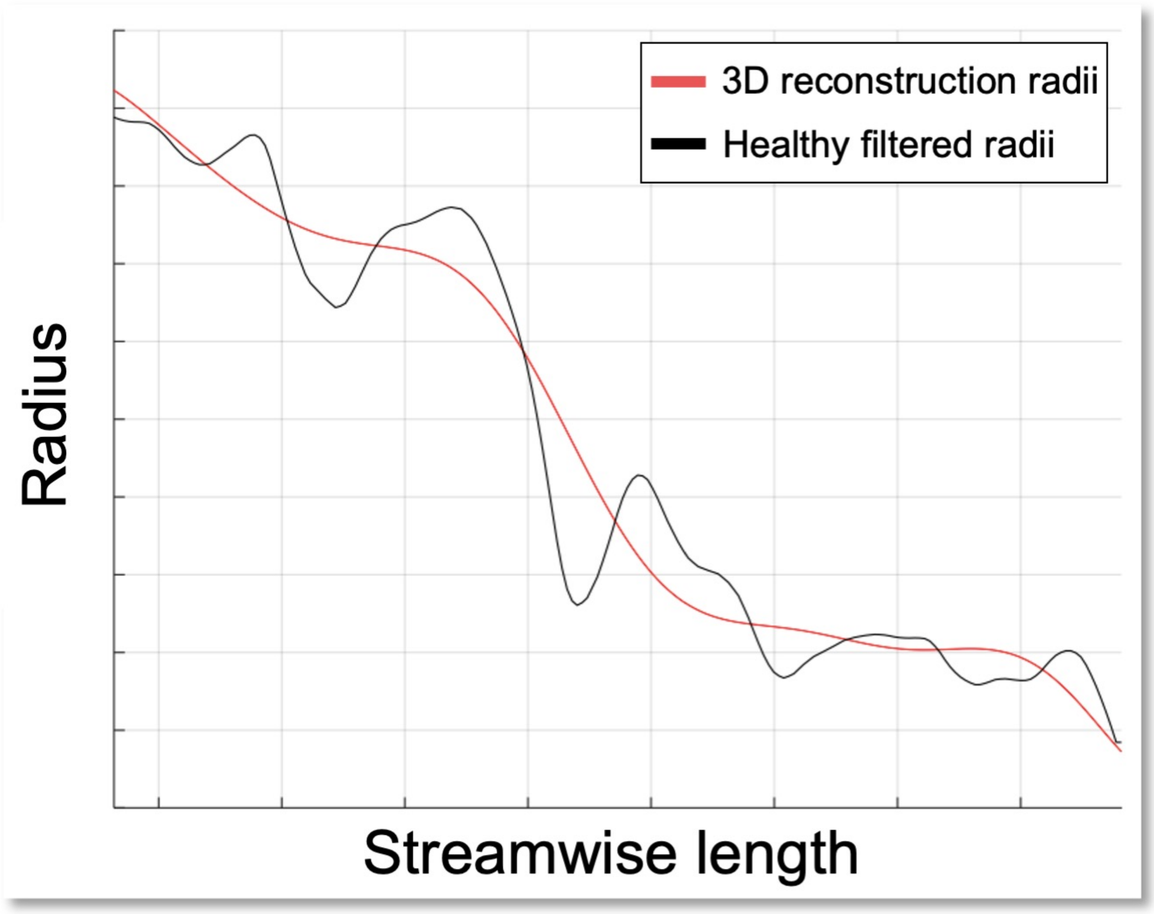


# Simulations and data analysis

## vFFR comparison

Taper vs standard 1D model

1500 total simulations
(100 per case)

Correlation and Agreement
assessed

## Sensitivity analysis

Taper model

vFFR and flow (mL/min)

Sobol indices for
1. All simulations
2. vFFR subgroups

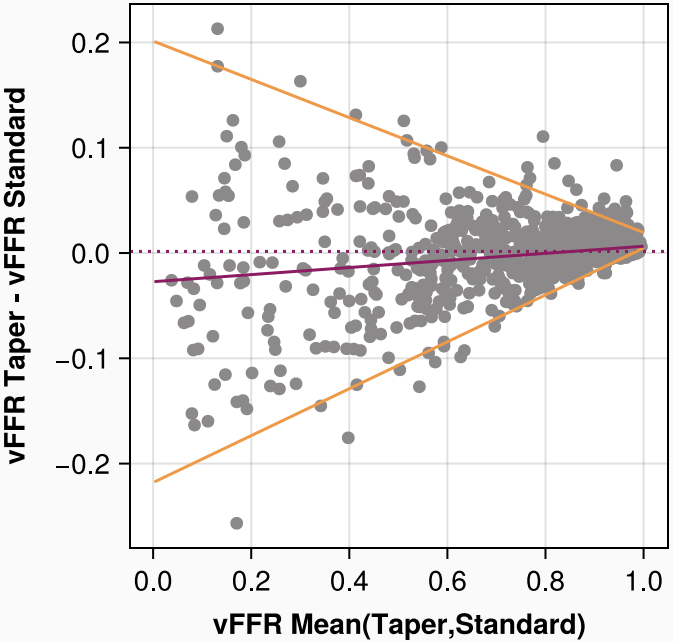


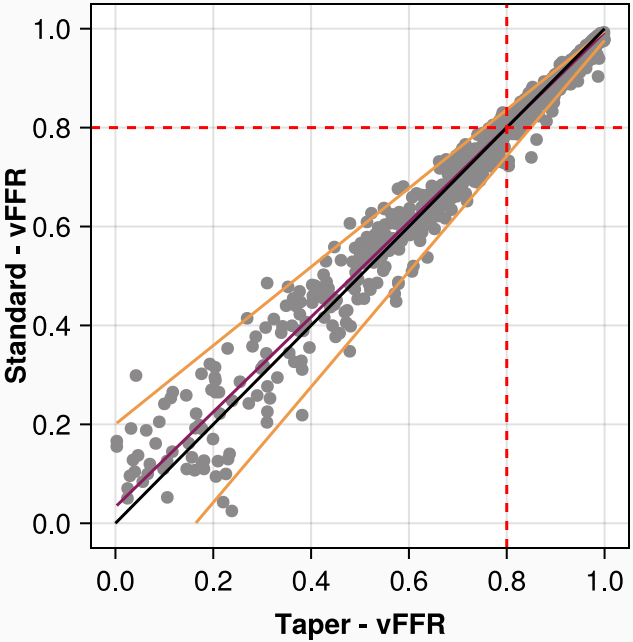


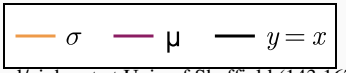

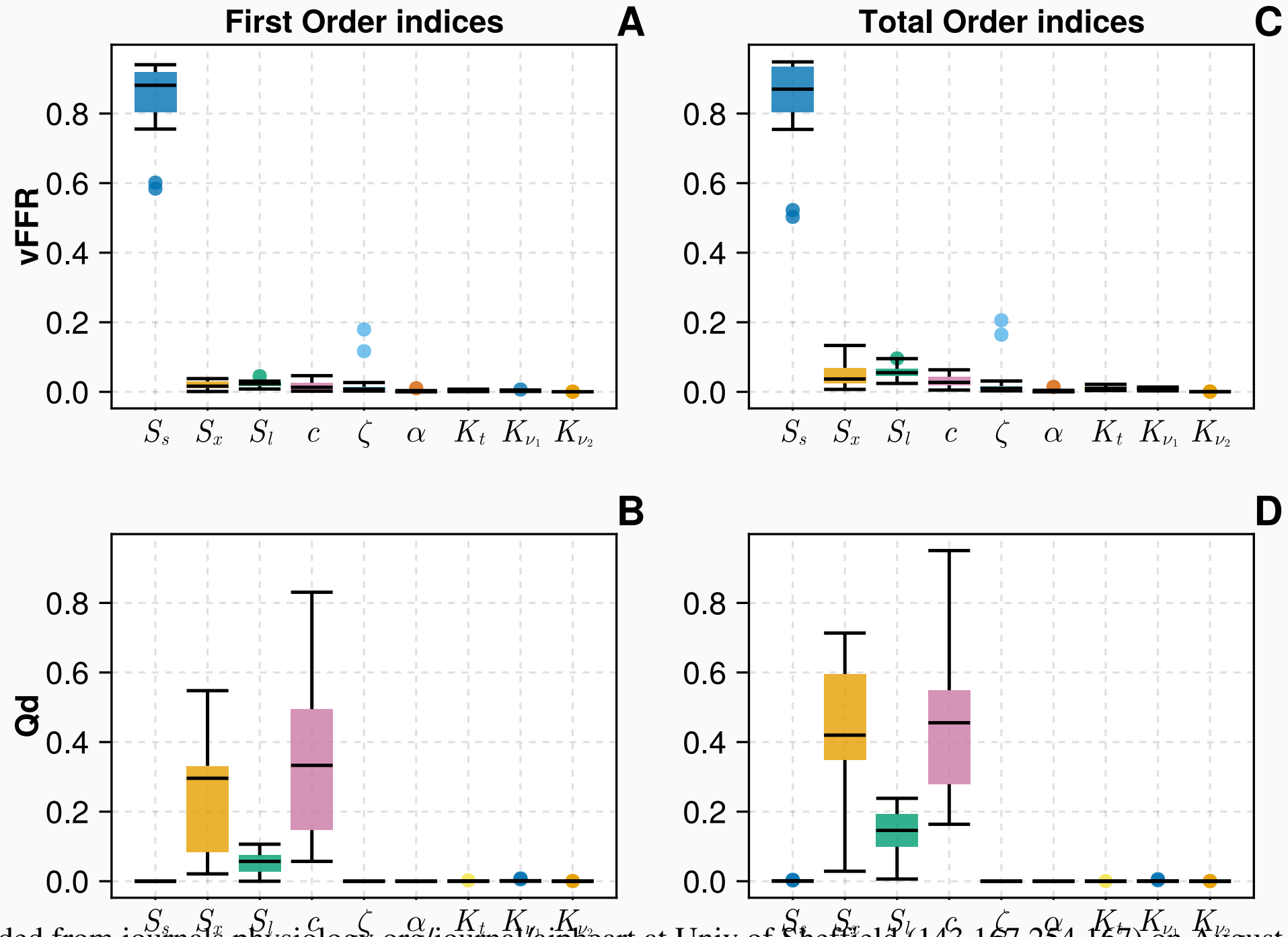

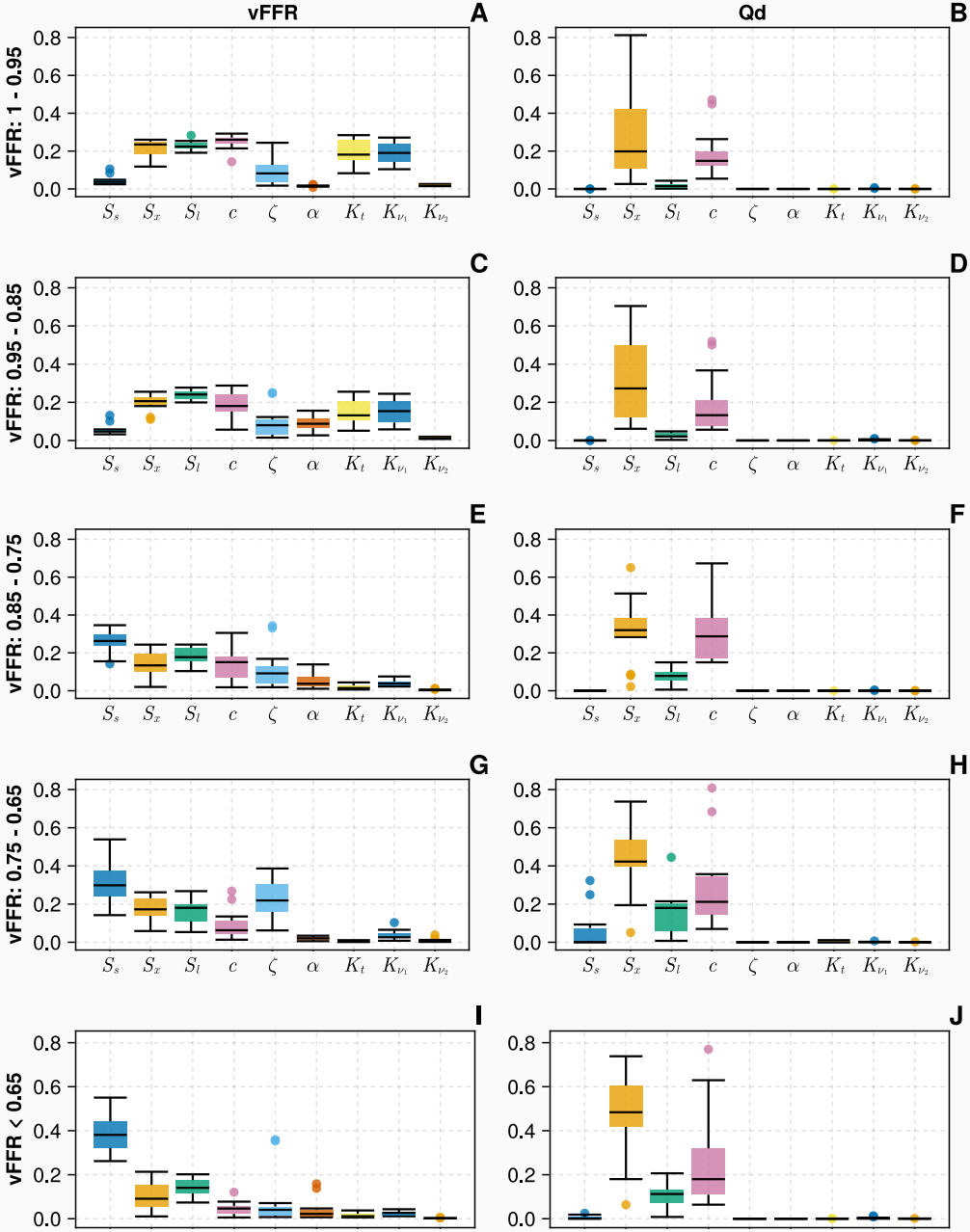

# Clinical Data Collection and Vessel Reconstruction

## Angiography & FFR

## Segmentation & 1D reconstruction

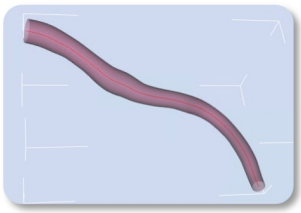

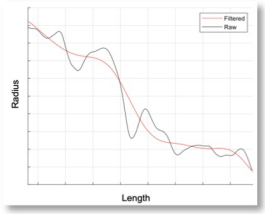


# 1D Taper Model of Flow Derivation

$$\frac{dQ}{dx} + \psi = 0,$$

$$\chi \frac{d}{dx}\left(\frac{Q^2}{A}\right) + \frac{A}{\rho}\frac{dP}{dx} + \frac{2(\zeta+2)\pi\mu}{\rho}\frac{Q}{A}\left(1+\left(\frac{dR}{dx}\right)^2\right)^{-1/2} + \alpha\frac{Q}{A}\psi = 0,$$

$$Q(0) = Q_{p,0},$$

$$P(0) = P_{p,0}.$$

# vFFR Comparison

## Taper vs Standard model

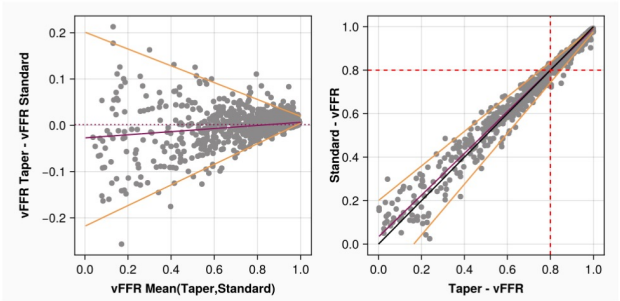


1314 comparisons in idealised geometries
r = 0.99 p<0.0001
Zero mean bias, 95% CI [−0.06, 0.06]

# Sensitivity Analysis

## Sensitivity of taper model
## 165 million model executions

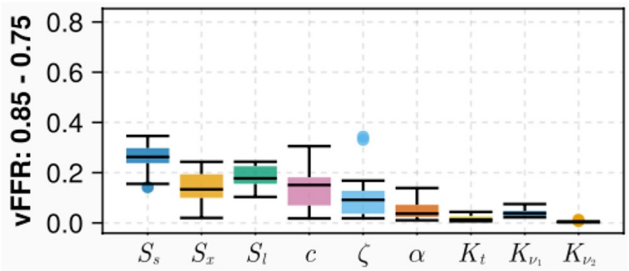


Murray flow diameter scaling exponent and anatomical accuracy influential in vFFR grey zone